41st AIAA Fluid Dynamics Conference and Exhibit
27 - 30 June 2011, Honolulu, Hawaii

AIAA 2011-3248

Roughness-Induced Instabilities at Mach 6: A Combined Numerical and Experimental Study

Bradley M. Wheaton*
School of Aeronautics and Astronautics, Purdue University, West Lafayette, IN 47907

Matthew D. Bartkowicz* and Pramod K. Subbareddy†
Department of Aerospace Engineering and Mechanics, University of Minnesota, Minneapolis, MN 55455

Steven P. Schneider‡
School of Aeronautics and Astronautics, Purdue University, West Lafayette, IN 47907

Graham V. Candler§
Department of Aerospace Engineering and Mechanics, University of Minnesota, Minneapolis, MN 55455

To develop improved methods of transition prediction for isolated roughness based on the growth of disturbances in the roughness wake, the underlying instability mechanisms must first be understood. This paper presents a direct comparison of experimentally-observed and computed instabilities due to a cylindrical roughness in a boundary layer at Mach 6, to identify the dominant mechanism for transition. Direct numerical simulations allow a detailed analysis of the entire flow field, while experimental measurements discover the real flow physics and confirm the findings of the computations. For a large roughness height of 10.2 mm, an instability with a frequency near 21 kHz originates in the separation region upstream of the roughness. Unstable shear layers and horseshoe vortices appear to cause transition downstream of the roughness for this case. As the roughness height is reduced, there appears to be a change in the dominant instability mechanism.

Nomenclature

δ	boundary-layer thickness ($0.995u_\infty$)
D	roughness diameter (5.97 mm)
k	roughness height
p	static pressure
p_0	stagnation pressure
p_{02}	pitot pressure (behind normal shock)
Re_k	Reynolds number based on roughness height k and local conditions in the undisturbed laminar boundary layer at the height k
x	streamwise coordinate
y	vertical coordinate
z	spanwise coordinate

Subscripts and Notation

∞	freestream condition
i	initial condition at start of run
$'_{\text{rms}}$	root mean square
$< >$	mean

Abbreviations

BAM6QT	Boeing/AFOSR Mach-6 Quiet Tunnel
CFD	Computational Fluid Dynamics
DNS	Direct Numerical Simulation
RMS	Root Mean Square

*Research Assistant, Student Member AIAA
†Research Associate, AIAA Member
‡Professor, Associate Fellow AIAA
§Professor, AIAA Fellow

I. Introduction

Laminar-turbulent transition is important in the design of hypersonic flight vehicles, as a turbulent boundary layer causes local increases in heat transfer and skin friction. The location of transition is influenced by many factors and is difficult to predict.[1] Transition is caused by disturbances within the freestream or on the body, which enter the boundary layer via receptivity mechanisms, grow through various instability modes, and cause turbulence.[2] Among the many factors that can influence hypersonic transition is surface roughness, which can cause transition to occur prior to the natural transition location.[3] From a design standpoint, it may be necessary to determine if a typical, as-built surface roughness will cause transition during reentry, or to determine the surface roughness magnitudes and distributions that will begin to affect the natural transition location. Isolated roughness elements can also be used to intentionally cause transition within a laminar boundary layer, for instance to prevent scramjet engines from unstarting.[4,5]

The physics of roughness-induced transition are poorly understood, and experimental measurements of roughness-induced instabilities at supersonic and hypersonic speeds are limited. An isolated roughness often generates a wake with streamwise vortices originating from within the separation region upstream of the roughness. Streaks from vortices were observed in oil-flow visualization by Whitehead in 1969.[6] Flow structures oriented in the streamwise direction have also been observed in recent high-speed experiments.[5,7,8] For large roughnesses ($k/\delta \approx 1.0$ or greater), the dominant instability type is likely to be an "absolute" instability. Absolute instabilities grow in time from an initial disturbance and are oscillatory in nature.[9] Examples of absolute instabilities include periodic vortex shedding, as observed in low-speed roughness experiments,[10] or some other instability caused by the large disturbance of the flow by the roughness. For smaller roughnesses (as the roughness height tends towards zero), it is likely that "convective" instabilities within the shear layers generated by the roughness become the dominant mode of transition. Convective instabilities are characterized by spatial growth as they are swept downstream and are subject to the effects of external disturbances.[11] Other possible transition mechanisms include that of transient growth,[12] interaction of streamwise vorticity from the roughness with the Görtler instability or stationary crossflow,[3] or modification of the receptivity of the boundary layer.[13]

Correlations for transition due to roughness are used out of necessity with some success for many flight vehicles. These correlations are based on parameters such as Re_k, the Reynolds number at the roughness height k based on conditions in the undisturbed laminar boundary layer at the height k.[14] If not used carefully, correlations can lead to larger-than-desired uncertainty in the predicted transition location.[15] Measurements taken in conventional ground facilities may be subject to tunnel noise effects, which can significantly alter the roughness-induced transition location.[16] Recent NASA flight experiments measured transition due to a controlled roughness on the heat shield of the Space Shuttle.[17,18] However, controlled measurements of transition in flight are often not available due to the high cost and difficulty inherent in acquiring them. The fact that empirical correlations are used despite sometimes large uncertainty highlights the need for better roughness-induced transition-prediction methods. Ideally, such prediction methods would be based on the growth of disturbances via instabilities within the roughness wake.[19,20] To date, the theory to enable development of such a method does not exist. Development of a new transition-prediction theory for roughness requires advancement in computational methods[21–24] together with controlled experimental measurements of instabilities.[25,26] This paper does not propose or advocate any particular theory, but rather attempts to characterize disturbances that have been observed experimentally in the wake of an isolated cylindrical roughness at Mach 6. Direct numerical simulations (DNS) performed here allow a detailed analysis of the entire flow field, while controlled experimental measurements are used to discover the flow physics involved in the transition process and confirm the findings of the computations.

II. Background

Experimental measurements of roughness-induced instabilities were obtained in the Boeing/AFOSR Mach-6 Quiet Tunnel (BAM6QT) at Purdue University and are the first known measurements of this kind at hypersonic speeds.[26–30] While most high-speed tunnels have a turbulent boundary layer on the nozzle wall, the BAM6QT can operate with a laminar boundary layer on the nozzle wall to eliminate acoustic noise generated from turbulent eddies. Lower noise levels are desired for transition research, but here the unusually thick laminar boundary layer on the nozzle wall is also of interest. At the conditions in these experiments, this laminar nozzle-wall boundary layer is on the order of 10 mm thick (an order of magnitude

thicker than typical hypersonic boundary layers on a wind-tunnel model). The unusually thick boundary layer is used to (1) increase spatial resolution, (2) reduce the effects of probe interference, and (3) reduce the instability frequencies such that instrumentation with relatively low frequency response can be used. The measurements here should complement similar work at supersonic conditions in the NASA Langley Supersonic Low-Disturbance Tunnel.[25]

Direct numerical simulations of experiments in the BAM6QT have been done at the University of Minnesota using the unstructured finite volume code US3D. Numerical solutions have the advantage of being able to unobtrusively examine the flow in great detail. It is difficult to include the effects of freestream noise, partly because of the difficulty in characterizing wind tunnel noise. By simulating a flow with a very low noise level this difficulty is avoided. However, it should be remembered that this difference may become important for some conditions.

In 2009, an instability was first detected using pitot and hot-wire probes at a frequency near 21 kHz.[26] To rule out stray effects from the probes, non-intrusive pressure sensors in the wake of the roughness were used to verify the existence of the instability.[29] Simultaneously, numerical simulations of the roughness wake near the experimental conditions found a disturbance of the same frequency and were able to predict the mechanism for creating the disturbance.[24] Prior to this paper, a quantitative comparison of the roughness-induced instability frequencies and amplitudes between experiment and computation has not been made. Such a comparison is the goal of the current work. In section III the experimental and numerical methods are described. Section IV presents results for a roughness with height $k = 10.2$ mm. Finally, the effect of changing the roughness height is explored in section V.

III. Methods

A. Boeing/AFOSR Mach-6 Quiet Tunnel (BAM6QT)

The BAM6QT[31] is one of two operational hypersonic quiet tunnels in the world, as the NASA Langley Mach 6 Quiet Tunnel[32] has recently been reassembled at Texas A&M University.[33] The design of the BAM6QT is that of a Ludwieg tube, consisting of a 37.3-m-long driver tube and a converging-diverging nozzle (Figure 1). During operation, the upstream portion of the tunnel is filled with high-pressure air at 433 K while the downstream portion is evacuated. The two regions are separated by double burst diaphragms, which are broken in rapid succession to initiate the flow. The tunnel Reynolds number decreases by approximately 15–20% during a typical quiet-flow run time of 3-6 s. The tunnel can be operated approximately once per hour at relatively low cost compared to traditional hypersonic tunnels. A laminar boundary layer on the nozzle wall (and also quiet flow) is achieved using several design features that delay transition,[31] though at high Reynolds numbers the boundary layer is still turbulent.

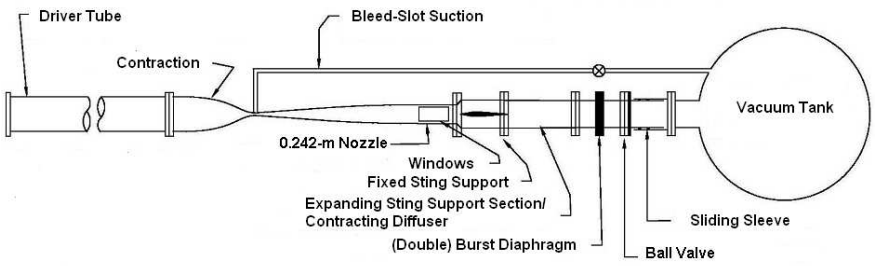

Figure 1. Schematic of the Boeing/AFOSR Mach-6 Quiet Tunnel.

B. Roughness

A 5.97-mm diameter micrometer head was used as the cylindrical roughness element, located on the nozzle wall at an axial distance of 1.924 m from the throat. The height k of the roughness can be adjusted from 0.00-24.31 mm with a precision of ± 0.05 mm. Because all measurements are taken along the tunnel centerplane, the roughness must be moved off the centerplane to measure instabilities off the centerline of the roughness wake. Various inserts allow the roughness to be placed 0.0, 0.5, 1.0, 1.5 and 2.0 roughness diameters (D) off

the tunnel center-plane. Measurements greater than $2.0D$ off the wake centerline are precluded by the cost of modifications to the tunnel hardware.

It should be noted that at an axial location of 1.924 m from the throat, the nozzle wall is still slightly expanding at an angle of 0.53°. Thus, there is a slight favorable pressure gradient present in the nominal boundary layer. The incoming boundary layer likely contains second-mode (or Görtler) instabilities; to date evidence of these has not been observed at the conditions of these experiments. It is likely that the second-mode instability amplitudes are low, with N-factors on the order of 1–2.[34] The Görtler instability amplitudes are predicted to be larger with N-factors of 4–6.

C. Kulite XCQ-062-15A Pressure Sensors

Kulite XCQ-062-15A pressure transducers were used as flush-mounted static pressure sensors on the nozzle wall, as well as in a pitot-probe configuration, to make dynamic measurements of roughness-induced instabilities. The sensor has a 1.68-mm diameter, a range of 0–15 psia, and uses strain gages on a silicon sensing element with a natural resonance frequency near 300 kHz. Two types of manufacturer-supplied screens can be used to protect the silicon diaphragm on the sensors.[35] In the pitot configuration, the more protective "B" screen results in a frequency response expected to be flat up to approximately 60 kHz. The less-protective "A" screen was used on the static sensors, with a superior frequency response estimated to be 90–120 kHz. The pressure sensors were calibrated in the tunnel using the vacuum that normally exists following a run as well as in a vacuum cell. The linear slope of the pressure-voltage calibrations agreed within 1–2% between different calibrations, however the intercepts varied and were not repeatable. At low static pressures of about 0.05 psia it is difficult to resolve the mean pressure with these 15-psia sensors, though the amplitudes of the pressure fluctuations can be measured using the slope of the calibration curve. As a result, the mean pressure must be taken from either the theoretical smooth-wall pressure, freestream pressure, or from the computations.

D. Configuration for Surface-Pressure Measurements of Instabilities

This section describes the first of two apparatuses used to make quantitative measurements of instabilities in the wake of the roughness element. Surface-pressure measurements are advantageous because they are not subject to possible interference effects from probes and allow simultaneous acquisition of data on many sensors. In this configuration the roughness is placed on the upper wall of the nozzle and the pressure sensors are placed on the tunnel centerplane along the upper wall. Figure 2(a) shows a schematic of the streamwise positions available for pressure-sensor installation with the approximate locations marked by dashes on the line above the schematic. The last section of the nozzle cannot easily be modified so the sensor locations are limited to various inserts. The sensors are placed in any of four locations: (1) near the roughness, as shown in Figure 2(b), (2) in a small circular insert approximately $20D$ downstream of the roughness, (3) a long insert placed in the slot normally used for probe insertion, (4) along the upper wall of the pipe insert downstream of the nozzle exit. The pipe insert is used to extend the 0.242-m diameter beyond the nozzle exit, and extend the location of the last sensor from $93.1D$ to $152.0D$ downstream of the roughness (from approximately 60δ to 100δ at $p_0 = 90$ psia). Experiments by Casper[36] have verified that the laminar boundary layer extends beyond the nozzle exit along the pipe insert – though with a greater likelihood of intermittent disturbances. These intermittent disturbances were not observed at the relatively low stagnation pressures in the present experiments.

E. Probe Measurements of Instabilities

A second apparatus allows measurements of instabilities within the flow (away from the wall) using either hot-wire or pitot probes. Both the Kulite pitot probe and hot-wire probes are similarly shaped and can be used interchangeably within the same apparatus, which is described in detail in Wheaton.[28] No recent probe measurements have been made, but comparisons will be made to pitot-probe data that has been reported previously.[26,28] In this configuration the roughness is placed on the lower wall of the nozzle and the probes are inserted through a slot on the upper wall. A long angled probe strut with a double-wedge cross section was designed to measure further upstream near the roughness. Figure 3 shows photographs of both the pressure-sensor apparatus and probe apparatus. The boundary layer in the nozzle is assumed to be axisymmetric such that measurements taken on the lower wall with the probes can be compared to

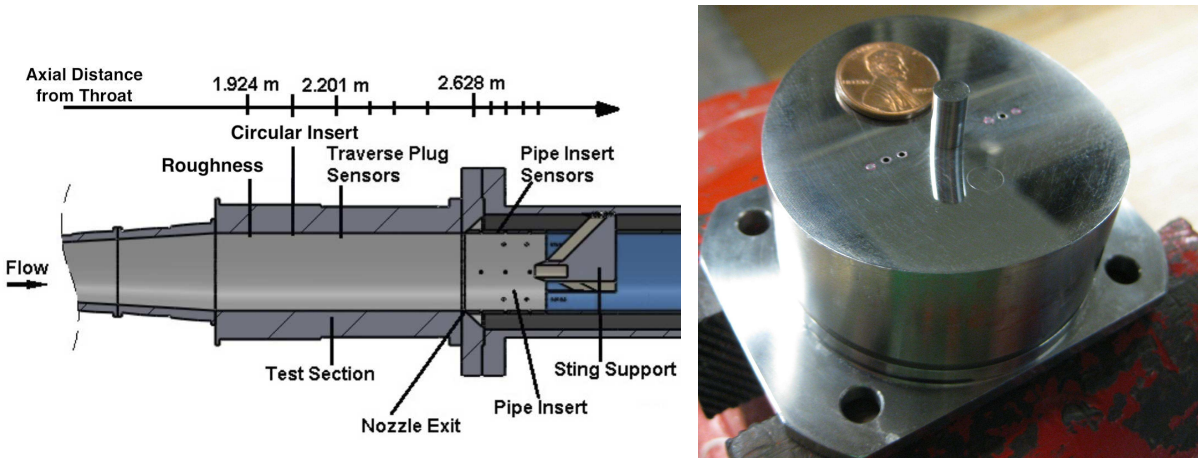

(a) Side-view schematic

(b) Roughness insert with pressure sensors

Figure 2. Apparatus for non-intrusive surface-pressure measurements: schematic of setup and roughness insert with pressure sensors (visible as dark spots on the surface).

measurements along the upper wall with the pressure sensors. For a quiet-flow run at $p_0 = 90$ psia, the Reynolds number decreases by approximately 10–15% in three seconds. For this reason, an accurate profile of the nozzle-wall boundary layer at a constant Reynolds number cannot be measured during a single run. A short tunnel run time limits the ability to make detailed measurements within the flow using probes, unlike similar NASA Langley experiments at supersonic conditions.[25]

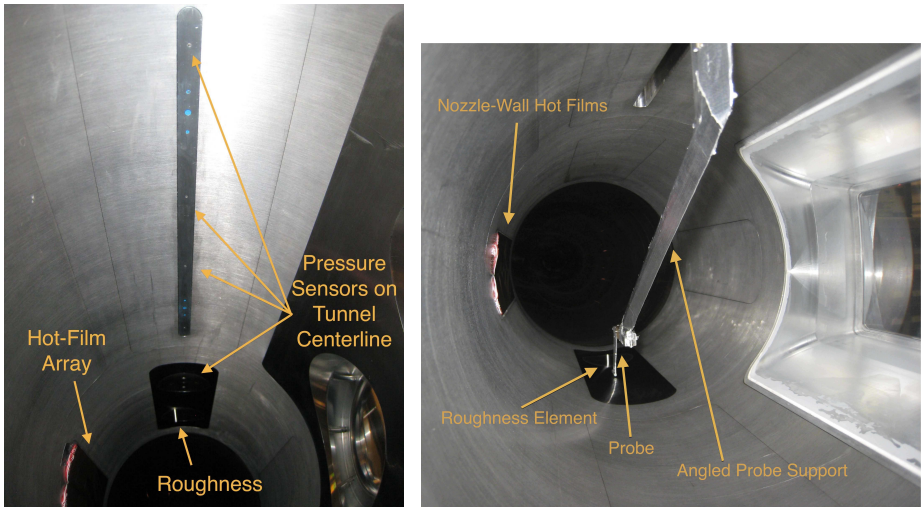

(a) Pressure-sensor apparatus

(b) Probe apparatus

Figure 3. View of pressure-sensor and probe apparatus looking upstream through the end of the nozzle.

F. Experimental Data Acquisition and Analysis

Probe and pressure-sensor data were sampled at 0.5 or 2.0 MHz in Hi-Res mode on a Tektronix DPO7054 Oscilloscope. Hi-Res mode is a method of digital filtering in which the scope samples at its maximum sampling frequency of 500 MHz and digitally averages in real time to the desired sampling frequency. This mode effectively acts as a low-pass filter to eliminate signal aliasing. In addition, Hi-Res mode decreases noise and increases the effective vertical bits of resolution. Experimental power spectra were computed using Welch's method to examine the frequency content of the signal. The spectra were computed from 0.1 second samples using Hamming windows with 50% overlap. The window size was 1/40 the number of points in

the 0.1-s sample for a total of 60 windows. Smooth-wall laminar and turbulent spectra were obtained from separate runs with no roughness using bleed suction to control the state of the nozzle-wall boundary layer. The pressure fluctuations from the roughness wake were nondimensionalized by the surface pressure at the sensor location from the computations. For smooth-wall data the fluctuations were nondimensionalized by the freestream pressure at Mach 6. The RMS pressure was obtained by numerically integrating the power spectrum over various frequency ranges of interest. The total RMS pressure was calculated by integrating from 0–100 kHz, in order to avoid effects of sensor resonance that occurred at higher frequencies.

G. Numerical Methods

A finite volume code is used to solve the compressible Navier-Stokes equations:

$$\frac{\partial \rho}{\partial t} + \frac{\partial \rho u_i}{\partial x_i} = 0 \tag{1a}$$

$$\frac{\partial \rho u_i}{\partial t} + \frac{\partial}{\partial x_j}\left(\rho u_i u_j + p\delta_{ij} - \tau_{ij}\right) = 0 \tag{1b}$$

$$\frac{\partial E}{\partial t} + \frac{\partial}{\partial x_j}\left((E+p)u_j - \tau_{ij}u_i + q_j\right) = 0 \tag{1c}$$

Where ρ, u_i, p and E are the density, velocity, pressure and energy. The viscous stress and heat flux are given by the following:

$$\tau_{ij} = \mu\left(\frac{\partial u_i}{\partial x_j} + \frac{\partial u_j}{\partial x_i} - \frac{2}{3}\frac{\partial u_k}{\partial x_k}\delta_{ij}\right) \tag{2a}$$

$$q_j = -\kappa\frac{\partial T}{\partial x_j} \tag{2b}$$

The viscosity is given by Sutherland's law in air and the heat conduction coefficient from the Prandtl number, assumed to have a constant value of 0.72.

The equations are solved using US3D, an unstructured finite volume code developed at the University of Minnesota.[37] The viscous fluxes are computed using a weighted least squares gradient approximation and deferred correction to approximate the gradients at cell faces. The inviscid fluxes incorporate a stable low-dissipation method developed by Subbareddy and Candler.[38] This is essentially a hybrid central/upwind scheme and is only briefly described here.

The inviscid flux is split into a central (non-dissipative) and an upwind (dissipative) portion. The upwinded portion is multiplied by a shock detecting switch that ensures numerical dissipation is only added in the regions needed for stability. The switch used in this paper is based on the switch put forth by Ren,[39] but uses density rather than characteristic variables. The dissipative portion of the flux comes from the upwinded portion of a Steger-Warming flux and is multiplied by the Ren switch.

A sixth order accurate gradient reconstruction is used to compute the central portion of the flux.

$$\phi_f = \frac{(\phi_L + \phi_R)}{2} + \frac{8(\delta\phi_L + \delta\phi_R)}{15} - \frac{(\delta\phi_{L2} + \delta\phi_{R2})}{45} \tag{3}$$

In this formulation ϕ is any variable being reconstructed at a cell face and $\delta\phi_i$ is the projection of the gradient of ϕ in cell i to the center of face f. L and R are the cells on either side of face f while $L2$ and $R2$ are on the opposite side of cells L and R. Thus, the second and third terms are a gradient extrapolation from both sides of face f that increases the stencil. The factors multiplying the gradients are chosen such that the modified wavenumber plot (on a one-dimensional stencil) has the same characteristics as a sixth order scheme.

A second order Crank-Nicolson scheme is used for time integration.

$$\frac{U_i^{n+1} - U_i^n}{\Delta t} = -\frac{1}{V_i}\sum_f \left(\frac{1}{2}F_f^n + \frac{1}{2}F_f^{n+1}\right)\cdot S \tag{4}$$

U and F_f are the solution vector and flux vector, respectively. The fluxes are linearized to obtain them at the $n+1$ time level and the implicit system is solved with the Full Matrix Data-Parallel method[40] which is fully parallelizable.

The wall is assumed to be isothermal with a temperature of 300 K. This assumption is discussed in greater detail in Section V. A time step $\Delta t = 5 \times 10^{-8}$ seconds is used: this corresponds to a CFL number near unity and ensures that the relevant time scales are resolved.

H. Grid Construction

The inflow boundary layer profile is an important parameter for simulating a flow of this kind. In order to obtain the correct boundary layer profile, a segment of the wind tunnel geometry (starting upstream of the nozzle throat) is simulated using an axisymmetric grid (size $2000 \times 1200 \times 2$) that adequately resolves the boundary layer as shown in Ref. 24. Note that this grid does not include the roughness element. The solution from this grid is used as the inflow condition for the full three-dimensional simulation.

The unstructured capability of US3D is important in these solutions. The ability to derefine the grid in regions away from the unsteady flow keeps the grid sizes manageable. Construction of the three dimensional grid for the roughness element calculations is done with the commercial gridding package GridPro. GridPro creates multiblock grids that allow for Cartesian-like grids in some areas but are also able to refine or derefine in regions. The grid has a high-resolution 'corridor' around the roughness element and its wake that can resolve the structures created by the presence of the cylinder. Away from this corridor, the grid is derefined quickly: this keeps the total grid size manageable. Figure 4(a) shows a part of the grid near the roughness element. Also note that using hexahedral cells (bricks) makes it possible to use the sixth order inviscid fluxes.

For the first part of this paper a very large domain is simulated which is able to capture the growth and evolution of disturbances created by the roughness element. It extends $25D$ upstream and $75D$ downstream of the roughness with a grid resolution of 32 points per diameter. This results in a grid size of 270 million elements. Previous numerical results[24] indicated that this was the required resolution to capture the 21 kHz instability (Figure 4(b)). However, this grid resolution study was for a slightly lower Reynolds number. As described later in this paper, the resolution may be slightly inadequate for the current conditions, though this is still being investigated.

The second part of this paper explores the effect of different roughness heights. By using the same grid topology and only changing the roughness heights, it is possible to quickly create the new grids. The simulations with varying heights explore the differences in the disturbances created by the roughness, so these grids only extend $10D$ downstream (and $25D$ upstream). They have the grid density of 32 points per diameter which results in grid sizes on the order of 30 million elements. For all grids, the first cell away from the wall is at a constant distance of 10μm which is within one wall unit.

IV. Instability due to a 10.2-mm Roughness

In this section results are presented for a roughness with a height of $k = 10.2$ mm at a stagnation pressure of $p_0 = 90$ psia. At these conditions, the roughness height is on the order of 1.2 times the boundary-layer thickness (δ, defined as the height at which the local velocity is 99.5% of the freestream velocity). The goal of this section is to document the instability mechanism responsible for transition in the particular case of this relatively large roughness. In section A a description of the flow is presented. Following that, in section B, are results showing an instability in the upstream separation region. Downstream pressure fluctuations are compared in section C and D and evidence for the flow becoming turbulent is shown in section E.

A. Flow Field Characteristics

An advantage to having CFD simulations along with experimental results is the ability of CFD to easily interrogate many aspects of the flow otherwise inaccessible to measurements. This is especially true in cases of transitional flow where attempts to make measurements in the flow can create disturbances that change the flow in question. The purpose of this section is to show the main flow features that can be inferred from experimental measurements, but cannot be directly observed.

Along the wall of the wind tunnel there is a laminar boundary layer with a weak but favorable pressure gradient. The roughness element creates a large adverse pressure gradient, causing the flow to separate. In this separation region (sometimes referred to as a separation bubble) a system of horseshoe vortices is created. Baker[41] described these vortices in great detail and, following his convention, we find that a six-vortex system is created. Streamlines which illustrate these vortices are shown in Figure 5(a). The flow is

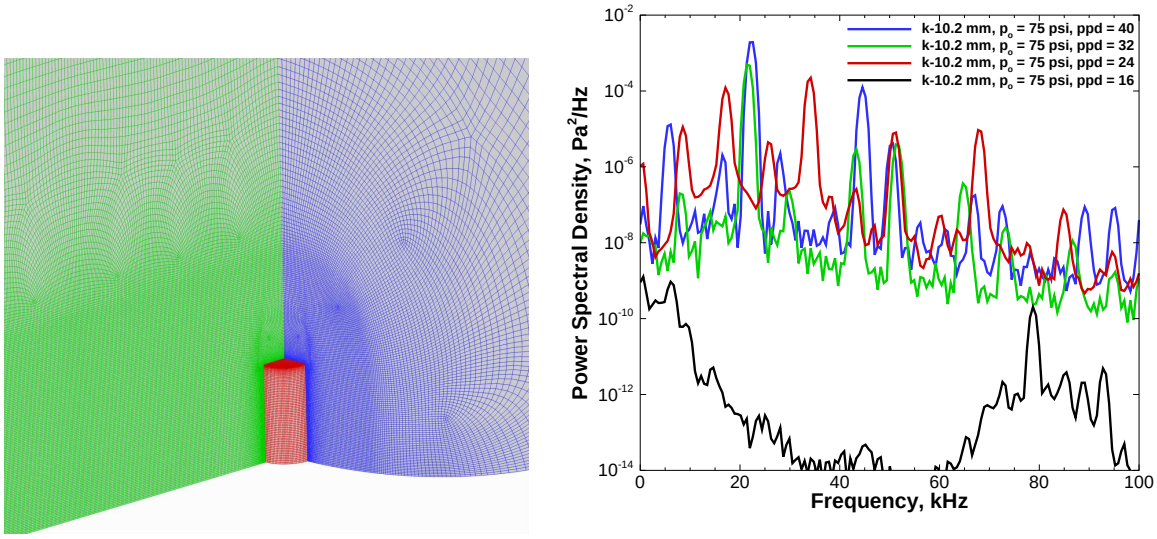

(a) Grid structure near the roughness element.

(b) Power spectra of the instability for several grid resolutions. Conditions are $k = 10.2$ mm and $p_o = 75$ psia.

Figure 4. The grid near the roughness element is dense, but is derefined elsewhere to keep total grid size manageable. Grid resolution study for $p_o = 75$ psia indicates 32 points per diameter is adequate.

from left to right. The coordinate y/D represents the height above the wall in roughness diameters while x/D represents the streamwise distance downstream of the roughness center.

The core flow of the wind tunnel is Mach 6 which means that a separation shock is created by the displacement of the separation bubble. This separation shock meets the bow shock formed from the roughness element extending into the flow and creates a λ-shock. Behind this bow shock is a large increase in pressure. This high pressure 'pushes' the flow down towards the tunnel wall where it gets entrained back into the separation bubble (Figures 5(b) and 5(c)). Unsteadiness created in this region is the mechanism for transition downstream and it is worth noting that this situation is very similar to the spike-tipped body instability.[42,43] There are essentially two stages in the unsteadiness: an inflationary stage and a collapsing stage. In the inflationary stage, flow behind the bow shock becomes entrained in the separation region. This causes the primary horseshoe vortex to grow while pushing the separation shock upstream. Due to the separation shock moving upstream, the normal shock weakens and pushes less fluid back into the separation region. This begins the collapsing stage in which the vortex shrinks and the separation shock moves closer to the roughness again, strengthening the bow shock and beginning another inflationary stage. The result is a 'breathing' of the separation bubble which creates disturbances that are sent downstream.

Downstream of the roughness element there are two main flow features. The first is the horseshoe vortex, which actually begins upstream and wraps around the roughness element and is carried downstream. The second is a shear layer that forms off the top of the roughness. Due to vortices in the wake, this shear layer gets bent down and in on itself, forming shear rings. Both of these features, the shear layer and the streamwise vortices of the horseshoe vortex, are inherently unstable. The unsteadiness of the separation bubble upstream sends disturbances downstream. At lower Reynolds numbers these disturbances are small and grow slowly downstream. At this condition, however, the disturbances are larger and the flow begins to transition almost immediately. Figure 6 shows iso-surfaces of the 'Q' criterion (second invariant of the velocity gradient tensor) in the vicinity of the roughness element and the vortical structures that form can clearly be seen. Figure 7 is a contour plot of temperature on the symmetry plane and shows the breakdown of the flow there. The next section will examine the frequency and amplitude of the instability on the surface upstream of the roughness.

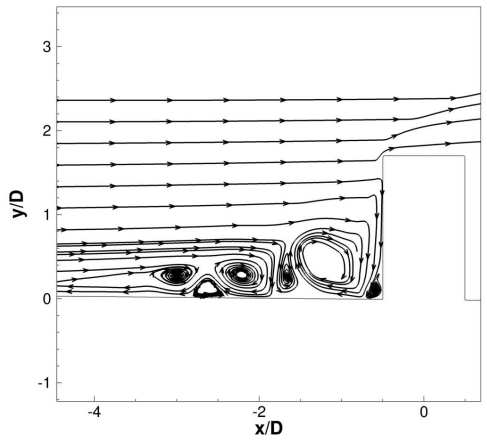

(a) Streamlines drawn on an instantaneous solution show the presence of multiple horseshoe vortices.

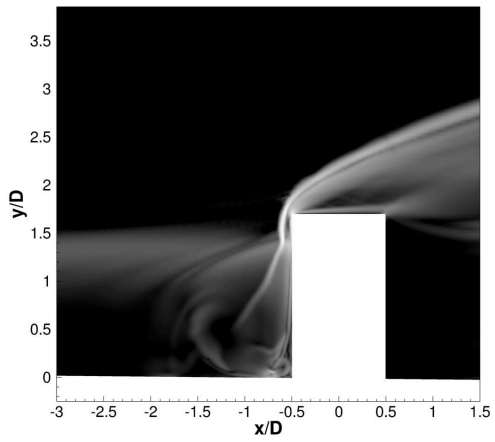

(b) Contours of density gradient magnitude are shown to illustrate the shock structure upstream of the roughness element.

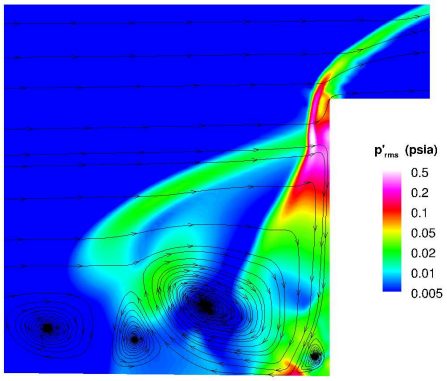

(c) Contours of RMS pressure along the centerplane upstream of the roughness, showing the oscillating shock structure and separation bubble. Streamlines are also plotted.

Figure 5. Streamlines, shock structure and RMS pressure upstream of the roughness.

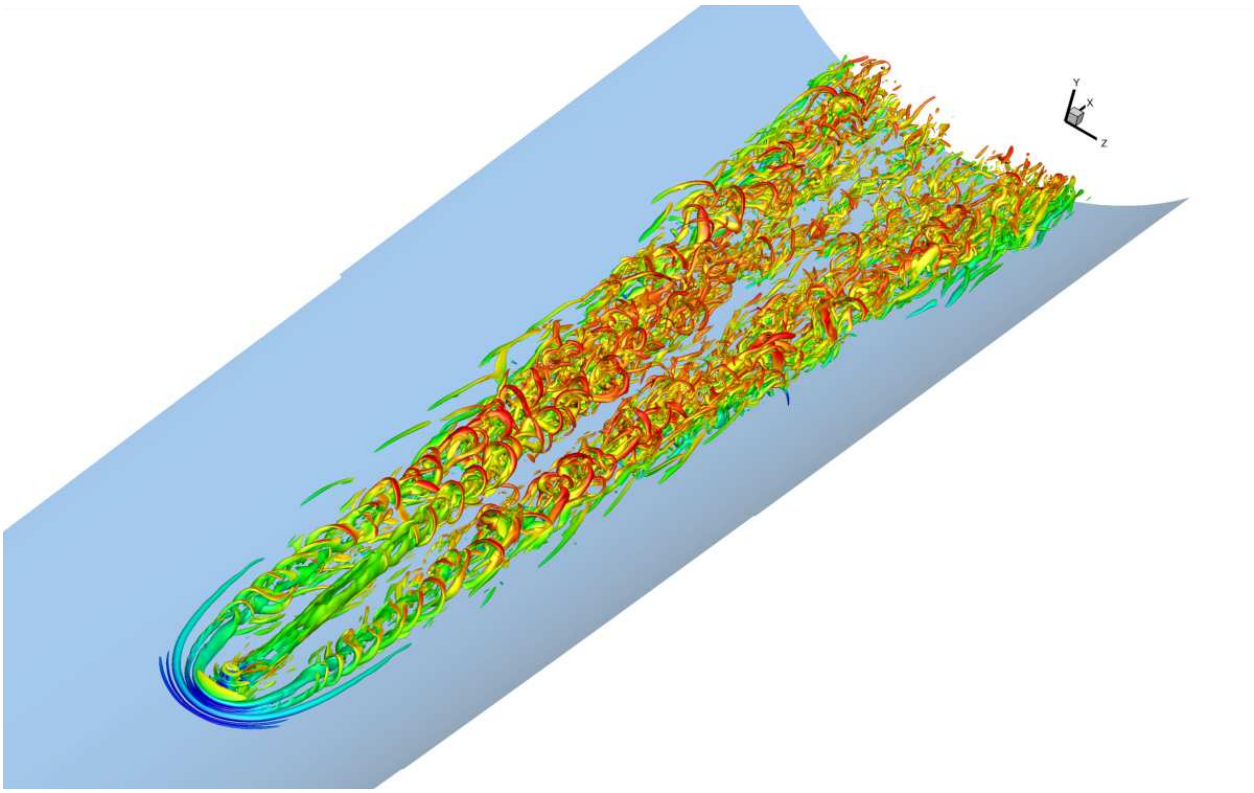

Figure 6. Iso-surfaces of 'Q' colored by streamwise velocity. Vortical structures can be seen forming in both the horseshoe vortex and the wake.

Figure 7. Contours of temperature on the symmetry plane show the breakdown of the shear layer.

B. Instability Upstream of the Roughness

Because the instability originates in the separation region upstream of the roughness, surface-pressure data were analyzed from both experiment and CFD at $x/D = -2.0$ and $x/D = -1.5$. Power spectra are plotted for both locations upstream of the roughness, as well as from experimental data taken in the absence of the roughness with a laminar and turbulent boundary layer (Figure 8). The experiments were performed from runs with an initial stagnation pressure $p_{0,i} = 95$ psia and a stagnation pressure of $p_0 = 90$ psia, to match the stagnation pressure in the computations. The legend in Figure 8 shows the RMS pressure (taken from integrating the frequency range of the instability peaks) nondimensionalized by the mean surface pressure. The frequency resolution of the spectra is 0.25 kHz for the experiments and 1.25 kHz for the CFD. Both the experiment and the CFD show the main peak for the instability, which occurs near 21 kHz for the experiment but at a slightly lower frequency of 18 kHz for the CFD. It is possible that the frequency is lower because the grid is not adequately resolved, as discussed in Section III. Both experiment and CFD show several harmonics, which are more clearly visible at $x/D = -1.5$. At $x/D = -2.0$ the experimental spectrum appears to have a lower peak amplitude but with fluctuations that are more broadband. The instability amplitudes show good agreement (2.7% vs. 1.9% at $x/D = -2.0$ and 6.6% vs. 6.4% at $x/D = -1.5$ for the experiment and CFD, respectively). At both sensor locations, the spectra are already near smooth-wall turbulent fluctuation levels even upstream of the roughness. It is unclear if this flow could be classified as turbulent solely due to these high fluctuations; large peaks from the instability still remain in the spectra.

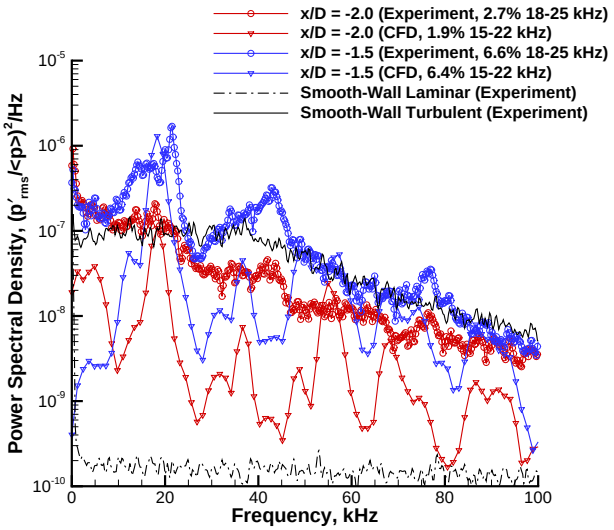

Figure 8. Power spectra from two sensors upstream of the roughness (both experiment and CFD).

C. Instability Within the Flow

A limited set of experimental pitot-probe data were available for comparison to the CFD results.[26,28] The data appearing here are at $x/D = 1.7$ and $z/D = 2.0$, where z is the spanwise distance from the center of the roughness. The data are from three separate runs with the probe traversing in the wall-normal direction. The probe initial height above the wall y_i was either 3.13, 15.13 or 23.13 mm and the probe movement direction was either towards or away from the wall. The probe was halted for 0.05 s at each point to collect data. Though the computations are at a constant stagnation pressure of 90 psia, the experimental conditions varied between $p_0 = 90$ psia and $p_0 = 77$ psia as the probe was traversed through the wake. It should also be noted that due to the curvature of the tunnel wall, when the roughness is placed $2.0D$ off the tunnel centerplane, measurements are actually made in a plane that is angled 5.7° with respect to the roughness. At a height of 15 mm above the wall the probe is actually at $z/D = 1.75$, or $0.25D$ closer to the roughness than it would be at the surface.

A profile of mean pitot pressure from both experiment and CFD is plotted in Figure 9(a), nondimensionalized by the freestream stagnation pressure. The CFD pitot profile was calculated from the mean flow using

conditions behind a normal shock when the local flow was supersonic. The profiles show good agreement except for a small region near $y = 11$ mm where the CFD results overshoot the experimental results. The experimental data points come from a 1.68-mm diameter pitot probe, so it is possible that the sensing element is too large to capture the overshoot. Away from the wall, both the experimental and numerical pitot pressures approach the theoretical value for Mach 6.

Figure 9(b) shows two quantities compared on the same axis: the RMS static pressure from the CFD results, nondimensionalized by the local mean static pressure, and the RMS pitot pressure from experiments, nondimensionalized by the local mean pitot pressure. It was not possible to plot RMS pitot pressure from the CFD at every grid point because a time history of the necessary quantities required to compute it were only recorded at a few points. A colored contour plot of the nondimensional RMS static pressure from the CFD results (in the spanwise plane of $x/D = 1.7$) is shown in Figure 9(c), along with black dots representing the approximate locations where pitot measurements were taken (though measurements were actually taken normal to the wall and not parallel to the roughness). It appears that the probe was moved through several flow structures of interest. At 4 mm from the wall, a peak in the CFD RMS pressure is seen from the main horseshoe vortex structure. A second peak at 8 mm from the wall is due to oscillations of the main bow shock from the roughness, and a third peak near 11 mm is due to oscillations of the shock from the upstream separation region. The pitot data do not show peaks at the exact same locations, however this could be due to the pitot and CFD data taken in slightly different planes (due to curvature of the tunnel wall as discussed previously). The pitot data show a peak at 6.5 mm that could be the main horseshoe vortex and another peak near 11 mm that could be due to the bow shock from the roughness.

At each experimental pitot-probe location, the power spectrum was integrated from 19–23 kHz to calculate the RMS pressure due to the 21-kHz instability.[26,28] The same procedure was applied to CFD time-history data from seven locations along the probe's approximate path. Note that since the instability frequency in the CFD was slightly lower (18 kHz), the CFD integration range was 15–24 kHz. The results are shown in Figure 9(d), nondimensionalized by the theoretical freestream pitot pressure. In the experiments, the instability was observed to be strongest at a height just above the roughness height near 11 mm, a similar location to where a peak was seen in Figure 9(b). The CFD time-history data do not show this peak, but this is likely due to the limited number of probe points available from the CFD. The CFD data show higher instability amplitudes than in the experiment closer to the wall. This disagreement could perhaps be due to probe interference effects near the wall.

Root-mean-square pressure, nondimensionalized by the local mean pressure, is plotted in Figure 10 for several spanwise planes at $x/D = 5$, 10, 15, 30, 50 and 70. The plots show the evolution of the disturbances in the flow. At five diameters downstream the strongest disturbances are concentrated within the shear region caused by the roughness. At ten and fifteen diameters downstream the strongest disturbances appear off the centerline within the horseshoe vortex structures, though a symmetric lobe-shaped region of disturbances can be seen within the shear layer. Note that near the roughness the disturbances are larger than those typically observed in smooth-wall transition (near 25% of the mean pressure). The disturbances decrease in amplitude past thirty diameters downstream, suggesting that the flow has transitioned.

D. Surface-Pressure Fluctuations

A set of pressure measurements at various points on the wall were available to compare to numerical results. The large computational domain extends a distance of $75D$ downstream. Within this domain there are three downstream sensors at 21.9, 46.3 and $63.3D$. Several different runs were performed with the sensors placed 0.0, 0.5, 1.0, 1.5 and $2.0D$ off the centerline. There are also data from three sensors near the roughness at 0.0 and $2.0D$ off the centerline.

Figures 11 and 12 attempt to compare all the sensor data to CFD results simultaneously. To compare all the data on the surface, the tunnel wall is plotted as a plane with the pressure fluctuations plotted as distance from the wall. Very good agreement is reached between the experiment and simulations.

Statistics were taken for roughly 250 flow times based on the roughness diameter and freestream velocity. This may not be enough time to be statistically converged – we are continuing to investigate – though longer averages should not change the results appreciably. At 0.0, 0.5 and $1.0D$ off the centerline (Figures 13(a), 13(b) and 13(c)) the agreement is very good, especially on the symmetry plane. There are fewer experimental probes available for comparison off the centerline, but the existing probes agree well. The simulations overpredict the pressure fluctuations very slightly which may be due to the fact that the conditions are not exactly the same; the stagnation condition for the simulation is 90 psia while the experiment

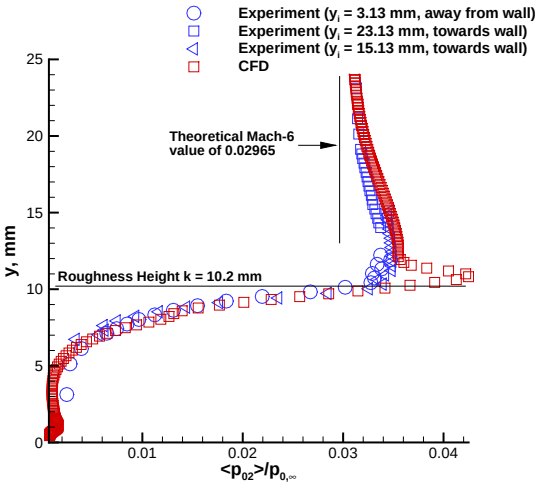

(a) Mean pitot pressure over stagnation pressure

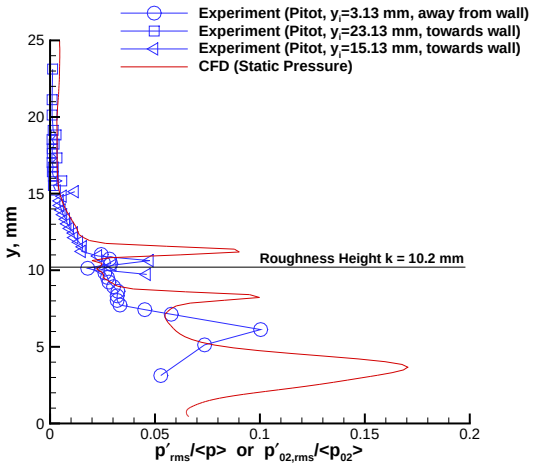

(b) RMS static (CFD) or pitot (experiment) pressure

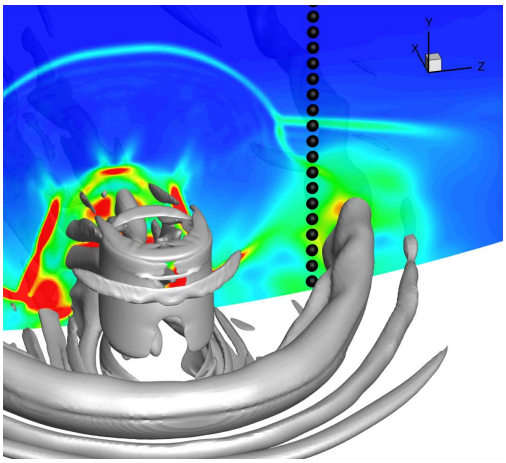

(c) CFD showing path of probe and RMS pressure in the spanwise plane of $x/D = 1.7$

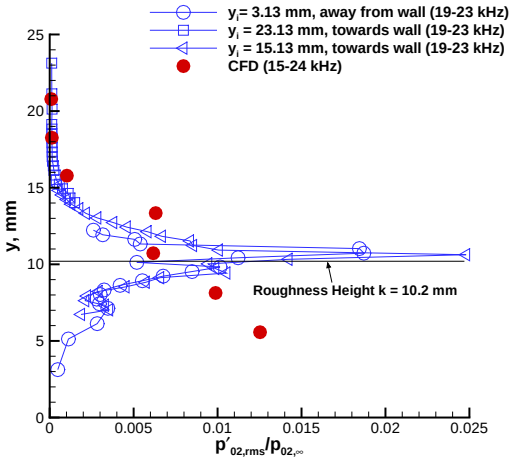

(d) Amplitude of instability peak compared to CFD

Figure 9. Comparison of pitot-probe data to CFD results at $x/D = 1.7$ and $z/D = 2.0$. The pitot-probe data are from three runs with the probe traversing in the wall-normal direction. Experimental conditions varied from $p_0 = 90$ psia to $p_0 = 77$ psia while CFD conditons constant at $p_0 = 90$ psia.

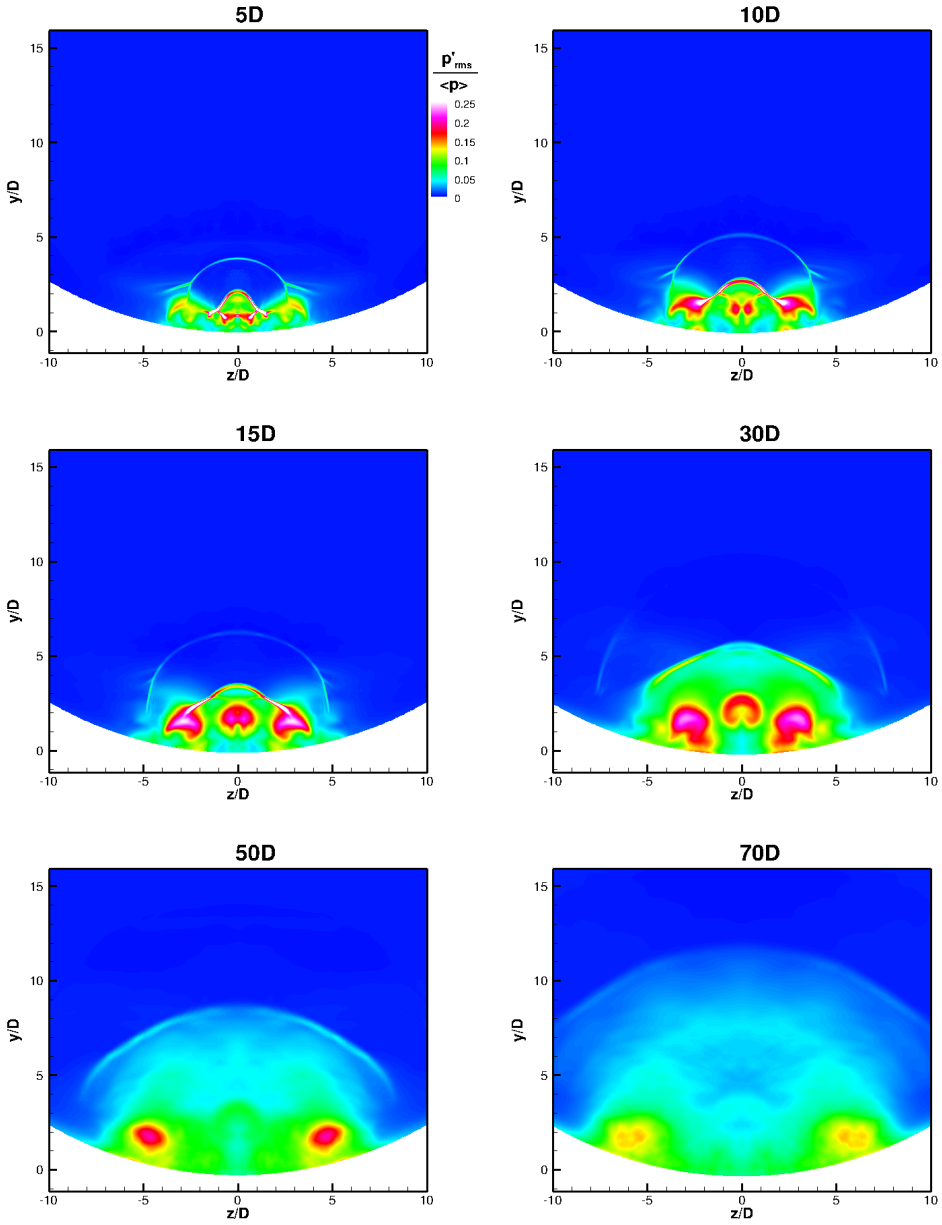

Figure 10. Contours of RMS pressure nondimensionalized by the mean pressure at various downstream locations.

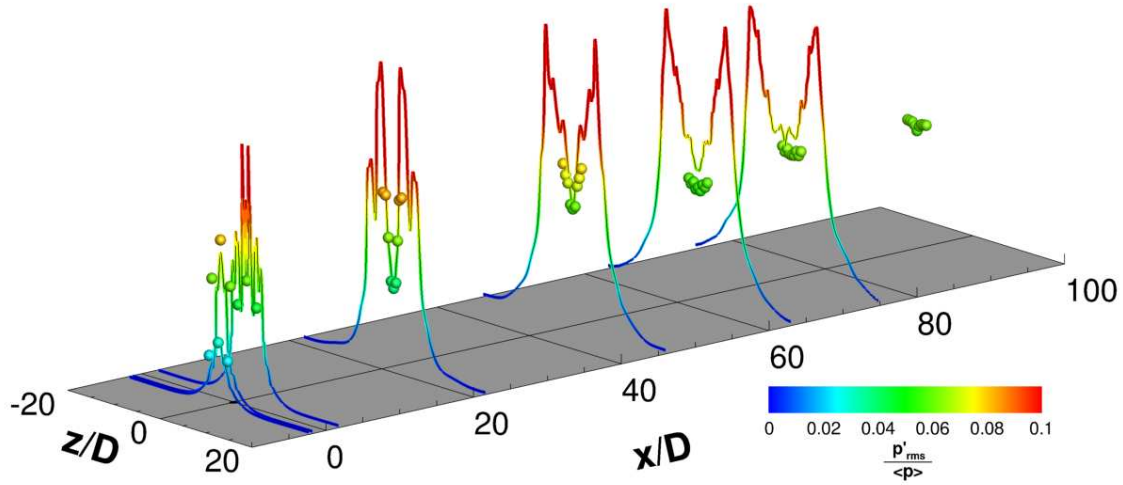

Figure 11. The tunnel wall has been unrolled onto the gray surface. The height above the wall and the color both represent the pressure fluctuations. The entire domain is plotted here. Lines represent the CFD data while the dots represent the experimental data.

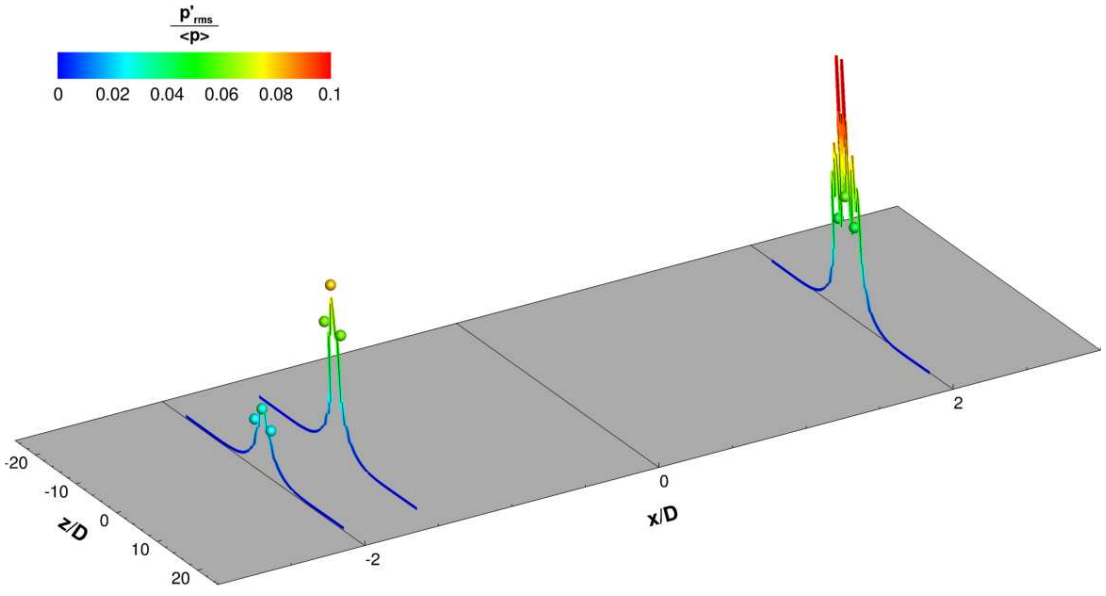

Figure 12. The tunnel wall has been unrolled onto the gray surface. The height above the wall and the color both represent the pressure fluctuations. Only a region near the roughness element is plotted here. Lines represent the CFD data while the dots represent the experimental data.

is 85 psia.

Off the centerline the agreement is not quite as good. Figure 13 shows the surface pressure comparison for these locations. At 1.5 and 2.0D from the centerline the overprediction of the CFD becomes more pronounced (Figures 13(d) and 13(e)). As before, this may be due to the slight discrepancy in stagnation conditions. A peak also develops in the CFD solution at roughly 30D. Unfortunately there are no experimental pressure sensors nearby for comparison. It would be interesting in the future to get additional experimental data in this region to see if the trend in the simulation is in fact present.

E. Evidence of Transition to Turbulent Flow

Near the end of the computational domain, at $x/D = 70$, there is some evidence that the flow is turbulent – although it is difficult to say whether or not it is fully turbulent. Van Driest transformed boundary layer profiles at several distances from the centerline compare well with turbulent profiles (Figure 14(a)). In these locations, 2D-5D off the centerline (essentially the location of the horseshoe vortices), the mean profiles appear to be turbulent and agree well with DNS data from Spalart[44] and experimental data from Murlis[45] of incompressible flat plate boundary layers. At spanwise locations greater than 5D the profiles do not appear to be turbulent.

Turbulence intensities 2D from the centerline also compare fairly well with DNS data from Spalart of a flat plate incompressible boundary layer. In Figure 14(b) data from the current work has been scaled by the ratio of density and density at the wall ($\hat{u_i} = \sqrt{\rho/\rho_w}(u'_{i,rms}/u_\tau)$). The streamwise component is slightly overestimated near the wall, while the other two components are slightly underestimated. Near the boundary layer edge they are all slightly overestimated. The reason for this is unclear, but it may be due to the curved wall or other three dimensional effects. The slightly unsmooth curves also indicate that the data may not be statistically converged. This will be looked into in the future.

Taken all together, this seems to indicate that for these conditions the flow does indeed become turbulent by 70D downstream. Evidence of turbulence is supported by examining the experimental surface-pressure spectra along the centerline and downstream of the roughness (Figure 15). At all locations downstream of the roughness, the instability peak disappears from the surface-pressure spectra and the fluctuation amplitudes appear quite similar to the those observed for a smooth-wall turbulent boundary layer.

F. Summary of Instability and Transition due to a 10.2-mm Roughness

For these conditions, the dominant instability appears to be caused by an unsteady shock interaction between the bow shock from the roughness and the shock from the separation region. The unsteady high-pressure area behind the bow shock sends fluid down and into the separation region, where it is entrained. The oscillation occurs at a frequency near 18 kHz in the CFD and 21 kHz in the experiments, resulting in unstable shear layers and an unstable horseshoe vortex structure. The instability frequency is slightly lower in the CFD, possibly due to the grid not being converged. However, good agreement between the experiment and the CFD suggest that the CFD hypothesis for the instability mechanism is valid. It is suspected that the flow is turbulent by 70D downstream of the roughness, as indicated by comparison to classical turbulent profiles and the breakdown of the vortical structures within the wake.

For large roughnesses such as in this case, it is likely that transition will always occur. Here, a "large" roughness is defined as a roughness of sufficient height to generate an absolute-like instability within the upstream separation region. Because no freestream disturbances were modeled in the CFD, the instability likely originates solely from the separation region created by the roughness. As the roughness height is reduced, one would expect the transition mechanism to change. This effect will be explored in Section V.

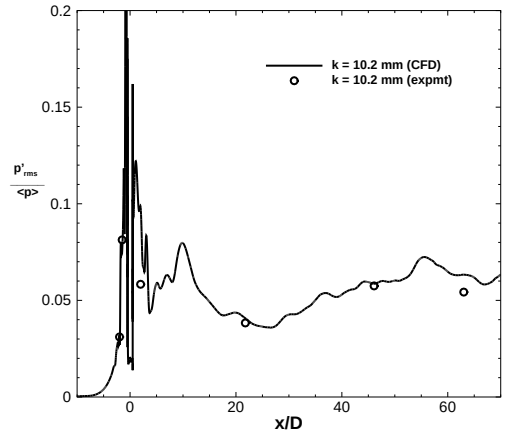

(a) Surface pressure fluctuations on the centerline.

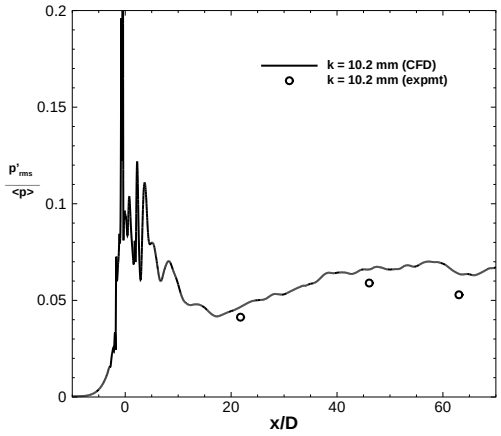

(b) Surface pressure fluctuations $0.5D$ off the centerline.

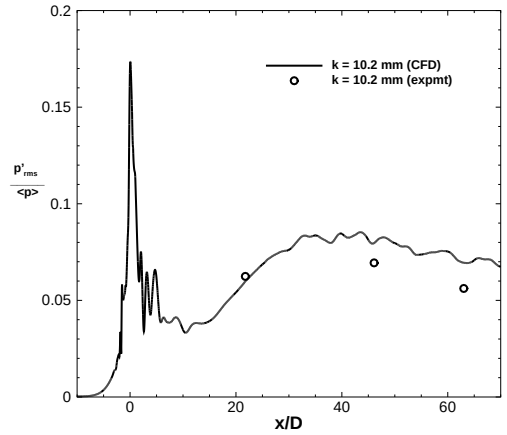

(c) Surface pressure fluctuations $1.0D$ off the centerline.

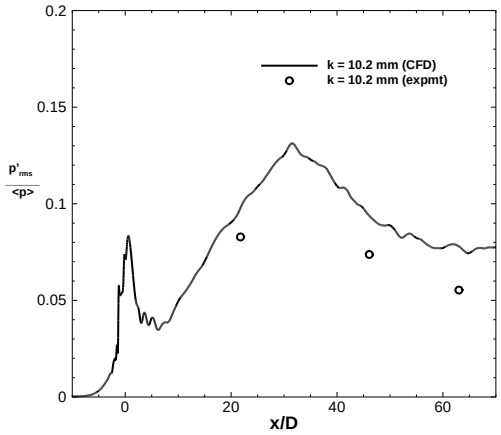

(d) Surface pressure fluctuations $1.5D$ off the centerline.

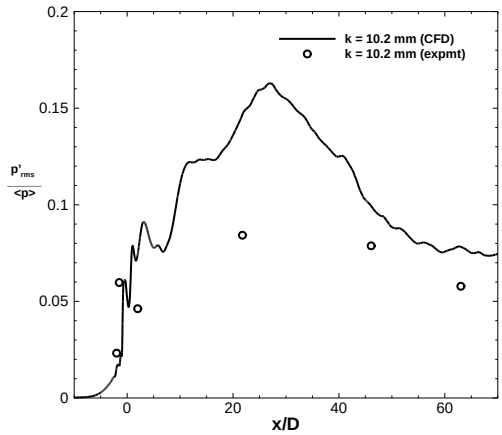

(e) Surface pressure fluctuations $2.0D$ off the centerline.

Figure 13. Surface pressure fluctuations normalized by mean pressure at several locations from the centerline.

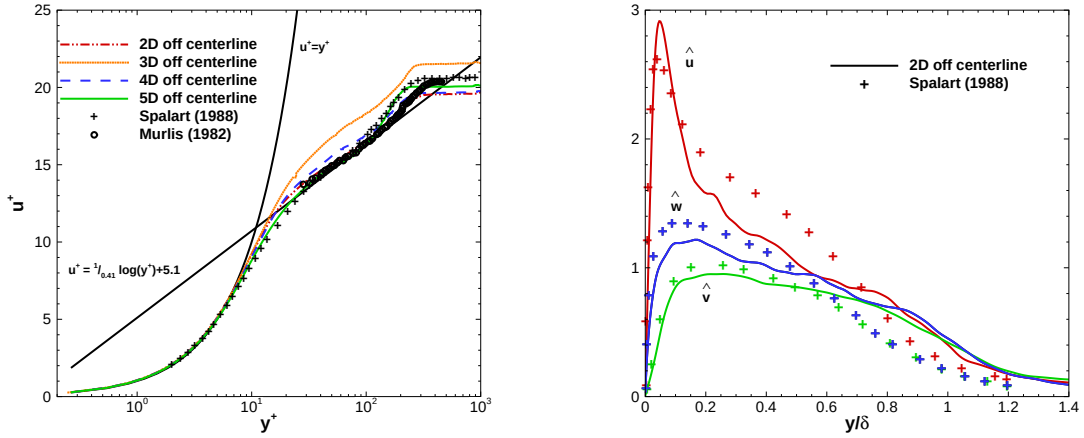

(a) Mean velocity profiles at $70D$ downstream and several locations off the centerline. Data is from Spalart (1988)[44] and Murlis (1982).[45]

(b) Turbulence intensities at $70D$ downstream and $2D$ off the centerline. Solid lines are from the current work with $\hat{u_i} = \sqrt{\frac{\rho}{\rho_w}}\frac{u'_{i,rms}}{u_\tau}$, data points are from Spalart (1988)[44] with $\hat{u_i} = \frac{u'_{i,rms}}{u_\tau}$.

Figure 14. Boundary layer profiles $70D$ downstream show good agreement with turbulent boundary layers.

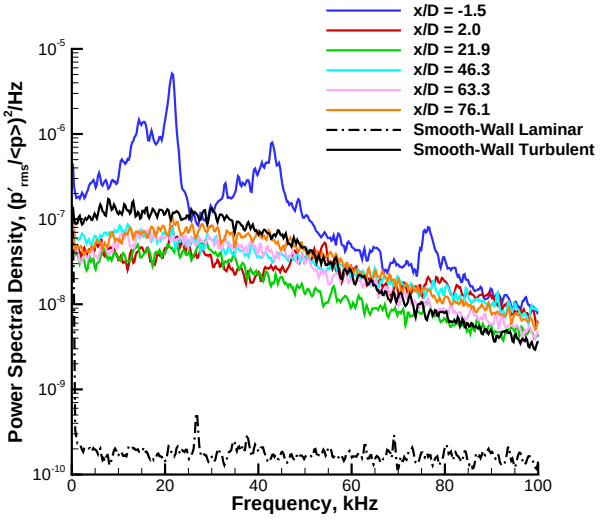

Figure 15. Experimental surface-pressure spectra along wake centerline ($p_{0,i} = 95$ psia, $p_0 = 90$ psia). Broadening of spectra downstream of the roughness suggests turbulent flow.

V. Effect of Roughness Height on Instability and Transition

The previous section has concerned instabilities occurring due to a fixed roughness height of 10.2 mm, and the corresponding instability mechanism developing in the upstream separation region when $p_0 = 90$ psia. This section will explore the effect of roughness height on the instability mechanism and the downstream wake for this fixed stagnation pressure. At a stagnation pressure of 90 psia, the undisturbed boundary-layer thickness (δ) at the location of the roughness is approximately 8.3 mm. Experimental measurements were taken for roughness heights between 1.8–10.2 mm and computations were performed for roughness heights of 7.4, 7.9, 8.4, 9.1, 10.2 and 11.2 mm.

A. Surface-Pressure Fluctuations Downstream of the Roughness

At stagnation pressures near 90 psia, a roughness height of 10.2 mm is on the order of 1.2 times the boundary-layer thickness. As the roughness height is reduced below this level, transition would be expected to move farther downstream. This trend was examined using pressure sensors along the wake centerline up to $x/D = 143.5$, or 100δ downstream of the roughness.

When examining solely surface-pressure spectra downstream of the roughness, it is difficult to qualitatively specify a location at which transition has occurred. Transition is normally inferred by a broadening of the instability peak and a rise in the broadband fluctuations in the spectrum. To give a better sense of where transition may be occurring for the various roughness heights, the pressure fluctuations downstream of the roughness were plotted. Figure 16(a) shows the root-mean-square pressure along the wake centerline for various roughness heights, nondimensionalized by the freestream pressure at Mach 6. The data are from runs beginning at $p_{0,i} = 95$ psia and data are taken at $p_0 = 90$ psia. The smooth-wall laminar and turbulent levels are shown for reference. Note that the RMS pressure is calculated only from the frequency range of 0–100 kHz, as measured by the pressure sensor.

Also shown in the legend of Figure 16(a) are values of Re_k for each roughness height, computed using the US3D results. Note that the US3D results used an isothermal 300 K wall condition from the throat to the end of the nozzle. In reality, the temperature at the throat is near 433 K and approaches 300 K somewhere within the first third of the nozzle. The exact temperature distribution in the nozzle is unknown. Re_k was also computed from the Harris code,[46] assuming a linear decrease in temperature along the nozzle. However, this assumption resulted in a wall temperature of 330 K near the roughness (higher than expected) and values of Re_k that were significantly different from US3D (by 5–40% depending on the roughness height). The US3D estimation of Re_k is expected to be more accurate due to a more accurate wall temperature at the roughness location. However, the uncertainty in the calculation of Re_k has yet to be quantified.

The variation of Re_k with roughness height at the test condition is shown in Figure 16(b), along with points representing the specific roughness heights in Figure 16(a). It is important to note that Re_k (or $\rho_k u_k k/\mu_k$) can decrease by several orders of magnitude as the height of the roughness is reduced. Compared to the boundary-layer edge, the density and velocity are much lower near the wall. There is also a temperature increase that causes an increase in the dynamic viscosity. Finally, as the roughness height k is reduced, Re_k decreases by definition. All four factors together cause a large decrease in Re_k as the roughness height is lowered.

For roughness heights of 10.2 and 9.1 mm, the pressure fluctuations become large upstream of the roughness (up to 20% of the mean pressure) and decrease downstream of the roughness. At smaller roughness heights, the fluctuations upstream of the roughness are lower, possibly due to a change in the transition mechanism. For both 10.2 and 9.1 mm, the pressure fluctuations decrease rapidly just downstream of the roughness and approach smooth-wall turbulent values. It is likely that for these large roughness heights the strongest fluctuations would be occurring somewhere off the wake centerline.

As the height is reduced from 7.4 mm to 3.8 mm, Re_k decreases by two orders of magnitude. However, these two cases show similar pressure-fluctuation amplitudes along the wake centerlines. It would not be expected that these two heights cause transition in a similar location. Again, it is possible that the wake changes significantly between these two cases and the measurements along the wake centerline may not accurately capture the locations of the maximum pressure fluctuations. Alternatively, the sensors may be spaced too far apart to detect differences between the two cases.

For the smallest roughness heights that are submerged deep within the boundary layer, the wake is expected to be thinner and the centerline measurements may more accurately show transition occurring. For heights of 2.4 mm and below, the pressure fluctuations do not begin to grow to turbulent levels until at

least $x/D = 60$. An overshoot of the smooth-wall turbulent RMS pressure is seen for some of these heights, likely due to the flow transitioning. Maximum values of pressure fluctuations are commonly observed during transition, for example in Ref. 47. When $k = 2.0$ mm, Re_k is approximately 170 and the fluctuations do not depart from laminar levels until $x/D = 130$. Finally, for $k = 1.8$ mm the entire wake appears laminar. Future experimental work will examine instabilities in the wake of smaller roughnesses that do not cause transition until well downstream of the roughness, such as $k = 2.0$ mm at this test condition. Note that heights between 2.0–2.4 mm appear to have a large effect on the transition location even though Re_k varies only between 170–250. It is possible that transition is particularly sensitive to roughness heights within this region, though these cases have yet to be thoroughly examined for repeatability.

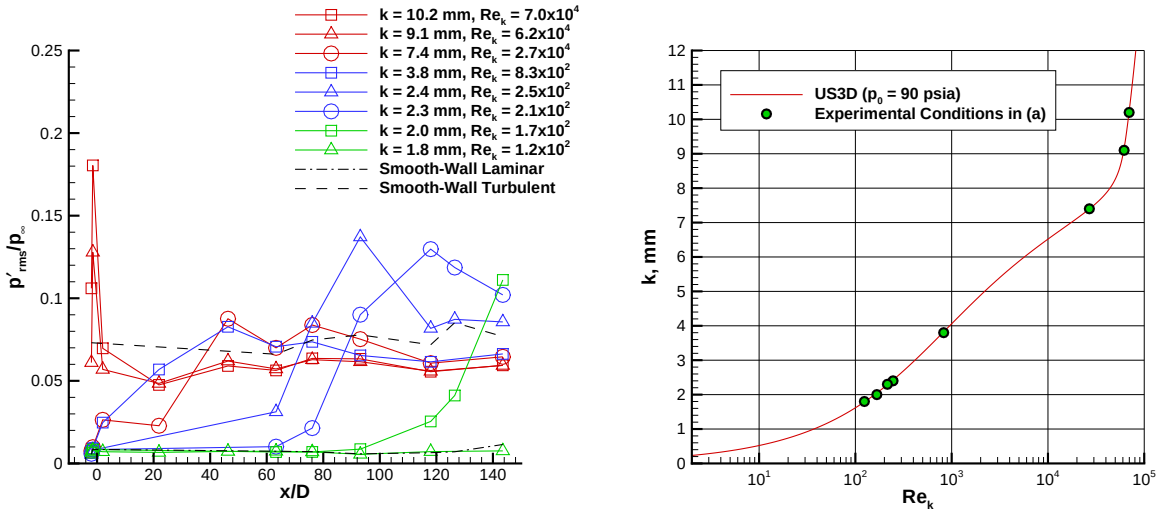

(a) RMS pressure along the wake centerline

(b) Effect of k on Re_k at $p_0 = 90$ psia

Figure 16. RMS surface pressure along the wake centerline for multiple roughness heights at $p_0 = 90$ psia.

B. Effect of Roughness Height on Instability Mechanism

Previous experimental work for a fixed roughness height of 10.2 mm observed a change in the dominant instability as the tunnel Reynolds number was varied.[30] At values of Re_k above approximately 5×10^4, the dominant instability occurred at a frequency near 21–22 kHz and was verified in computations.[24] The frequency of this instability was not observed to vary greatly with Reynolds number. Below $Re_k \approx 5 \times 10^4$, the dominant instability occurred at higher frequencies of 40–70 kHz and had a frequency that varied greatly with Reynolds number. As the Reynolds number decreased, the frequency of the higher-frequency instability also decreased. This second instability was not observed in the computations, which showed steady flow at the conditions of the experiments. Both types of instabilities were observed experimentally to occur upstream of the roughness within the separation region. Based on the results for a constant roughness height, a similar change in transition mechanism would be expected for a constant Reynolds number as the roughness height (and thus Re_k) is reduced.

1. Experimental Measurements in the Upstream Separation Region

The mechanism responsible for transition also appears to change for a fixed unit freestream Reynolds number as the roughness height is reduced. Figure 17 shows experimental power spectra from $x/D = -1.5$ (upstream of the roughness) from various runs with different roughness heights k. For this figure only every fourth point in the spectra are plotted for clarity. For each run, the initial stagnation pressure was 95 psia and the stagnation pressure was 90 psia. At this condition, the boundary-layer thickness, δ, is approximately 8.3 mm.

At the largest roughness heights of 10.2 mm and 9.7 mm, the spectra upstream of the roughness appear almost the same with the familiar peak near 21 kHz and several harmonics. It is possible that these spectra

are similar as a result of the roughness being beyond its effective height. As the roughness height is reduced, the peak frequency increases slightly to 24 kHz as the peak narrows and begins to disappear. A large peak appears near 75 kHz at a height of 9.4 mm. This higher-frequency peak appears to decrease in frequency as the roughness height is reduced further. This decrease in frequency is a similar trend as for a constant roughness height as the Reynolds number was decreased. As the height is reduced to 8.1 mm, the broadband fluctuation levels decrease to nearly-laminar levels though the narrow instability peak still remains near 58 kHz. Two runs were performed for the 7.9-mm case that show good repeatability of the peak amplitude and frequency. The peak frequency continues to decrease until $k = 7.4$ mm, at which point the boundary layer appears steady at $x/D = -1.5$ (though preliminary evidence suggests instabilities appear downstream of the roughness at this height). The steady boundary layer upstream of the roughness could signal another change in the instability mechanism, or the separation region may move too close to the roughness to be measured with this sensor. The trends in Figure 17 appear consistent with trends observed for a fixed roughness height of 10.2 mm at various Reynolds numbers.[30] At a condition somewhere near $Re_k \approx 6 \times 10^4$, the dominant instability mechanism appears to change. Future work will more thoroughly examine the spectra downstream of the roughness.

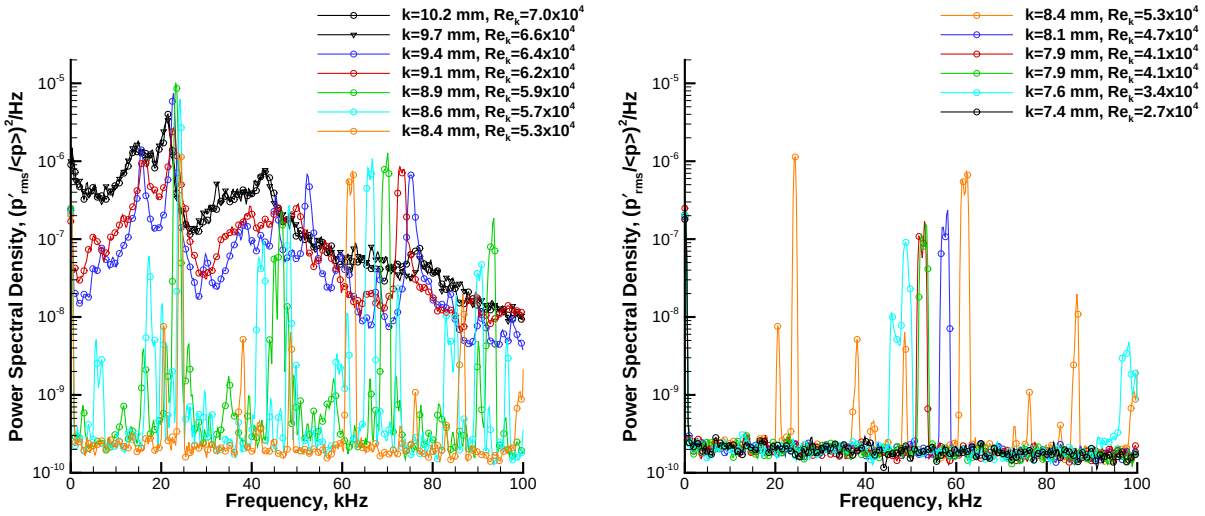

(a) $k = 8.4$–10.2 mm

(b) $k = 7.4$–8.4 mm

Figure 17. Effect of roughness height on instabilities upstream of the roughness. Spectra from $x/D = -1.5$ for several runs where $p_{0,i} = 95$ psia, $p_0 = 90$ psia, and $\delta = 8.3$ mm.

2. Computations of Various Roughness Heights

Computations were performed at a stagnation pressure of 90 psia for roughness heights of 7.4, 7.9, 8.4, 9.1, 10.2 and 11.2 mm. The grids for these simulations extend upstream to $x/D = -25$ and downstream to $x/D = 10$ to maintain manageable grid sizes and maximize the number of cases that could be simulated. These smaller grids seemed to be justified for these cases as experimental results showed the flow transitioning shortly downstream of the roughness, with the mechanism for transition existing in the separation upstream of the roughness.

Figure 18 shows iso-surfaces of the 'Q' criterion colored by the local non-dimensional velocity. In the case of the 11.2-mm roughness the disturbances created by the oscillations of the separation region can clearly be seen as hairpin shaped vortical structures convecting downstream in the horseshoe vortex. These disturbances are also seen in the wake directly behind the roughness element where the flow looks to be very unsteady. For the 10.2-mm roughness height, the main difference appears to be the width of the horseshoe vortex. This is most likely due to differences in the bow shock off the leading upper edge of the roughness. As the height is lowered, less of the element is exposed to the supersonic freestream. This results in less of the high pressure region that turns the flow back upstream into the separation region. For this height, disturbances in both the horseshoe vortex and wake are still visible.

As the height is further reduced to 9.1 mm, the width of the horseshoe vortex is also reduced. The disturbances can still be seen in the horseshoe vortex, but the wake appears to be laminar – or nearly so. At 8.4 mm the horseshoe appears to be significantly weaker and the size of disturbances in this region are much smaller. The wake appears to be more steady as well.

In the two lowest heights the wakes appear to be completely laminar. Although the heights remain above the sonic line, the normal shock created is continuing to become weaker. This results in the horseshoe vortices becoming weaker as well. The 7.9-mm roughness continues to show very small disturbances in the horseshoe vortex while the shortest height, 7.4 mm, is completely laminar and steady.

Figure 19 shows the RMS surface pressure along the centerline for each case, just upstream and downstream of the roughness. Experimental measurements are plotted as colored dots for comparison. The pressure fluctuations decreases as the height is reduced; this trend was observed in both CFD and experiment. In addition, as the height is reduced the extent of the separation region grows smaller and moves closer to the upstream edge of the roughness.

3. Comparison of Instabilities Between Experiment and Computation

Spectra from the experimental surface-pressure measurements at $x/D = -1.5$ were compared to CFD time-history data from the same location, in an effort to observe the change in the dominant instability mechanism as the roughness height is reduced. The CFD data were a time-average from five probes across the area of the experimental sensor face (CFD 'probes' are time histories of the solution in a grid element. Because the sensors are larger than the grid elements, several of these grid elements are averaged to approximate the actual sensor).

A comparison of experimental and computational spectra for five roughness heights is shown in Figure 20. The legend entries show approximate instability amplitudes taken by integrating under the instability peaks. Note that no experimental data were available for the 11.2-mm case. Smooth-wall laminar and turbulent spectra obtained from the experiments are also plotted. The laminar spectrum shows approximate noise levels in the experiments. The noise levels in the experiments are higher than in the computations since freestream noise effects were not simulated. The experimental trends are the same as discussed previously in Figure 17: as the roughness height is reduced, the instability near 21–22 kHz disappears and a new higher-frequency instability appears as broadband fluctuation levels are reduced. As the height is reduced from $k = 10.2$ mm to $k = 8.4$ mm the instability frequency increases by roughly 4 kHz and the amplitude decreases slightly. A similar trend is observed in the computations. In the computations, as the roughness height is reduced the peak frequency increases from 18 kHz to 25 kHz and the amplitude of the peak decreases. At the largest roughness heights of 10.2 mm and 11.2 mm, the spectra from both experiment and computation are near the smooth-wall turbulent amplitudes. However, as the roughness height is reduced the main instability peak near 18–25 kHz does not disappear in the computations until $k = 7.4$ mm. Instead, the peak remains along with harmonics as the broadband fluctuations decrease below the experimental noise levels.

A detailed comparison of the spectra shows that good agreement of the dominant instability in the separation region is obtained for the larger roughness heights (Figure 21). When $k = 10.2$ mm the fluctuations are near smooth-wall turbulent levels. The peak frequencies as well as the harmonic frequencies show slight disagreement. When $k = 9.1$ mm the broadband noise of the computations decreases below the experimental noise floor, but the peaks and harmonics remain strong. An additional peak is seen at 5 kHz, but is not as strong as the 22-kHz peak. The 22-kHz peak and harmonics remain strong when $k = 8.4$ mm, though several other peaks appear in the experiment that are not seen in the computations. When $k = 7.9$ mm, good agreement was not obtained for unknown reasons. At this height, the peak near 21–22 kHz disappears completely from the experiment and a new peak at 50 kHz appears along with a harmonic. In the computations, however, a large peak near 25 kHz is still visible. Finally, when $k = 7.4$ mm both experiment and computation show steady flow at $x/D = -1.5$.

The differences between experiment and CFD are likely due to freestream noise effects that are not present in the simulations. It is possible that the large instability near 21–22 kHz occurring at higher roughness heights is not sensitive to external disturbances and is an absolute-type instability. The instability at higher frequencies (occurring for lower roughness heights) could be more sensitive to external disturbances that cause it to grow to large levels in the experiments.

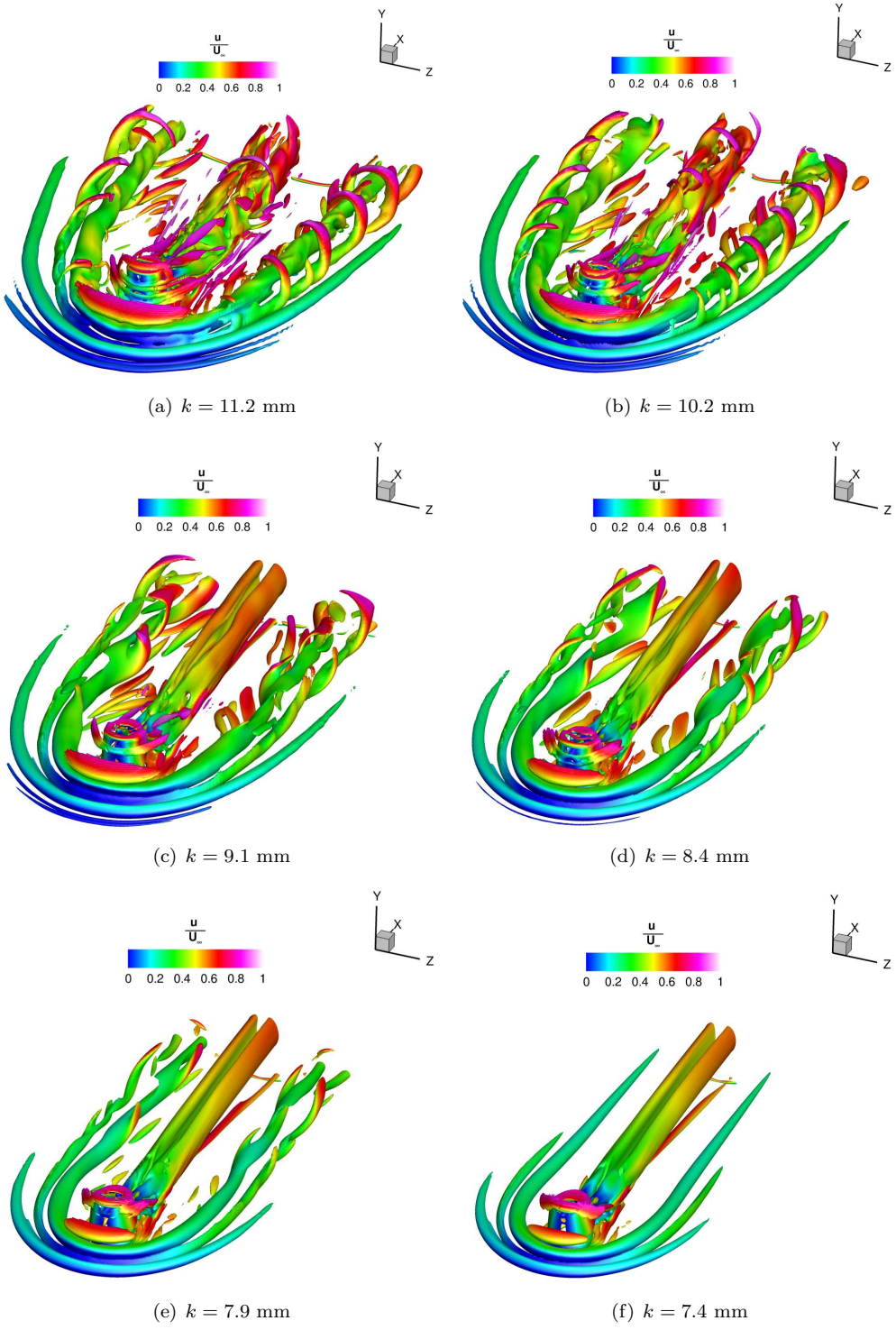

(a) $k = 11.2$ mm

(b) $k = 10.2$ mm

(c) $k = 9.1$ mm

(d) $k = 8.4$ mm

(e) $k = 7.9$ mm

(f) $k = 7.4$ mm

Figure 18. Isosurfaces of 'Q' for each roughness height.

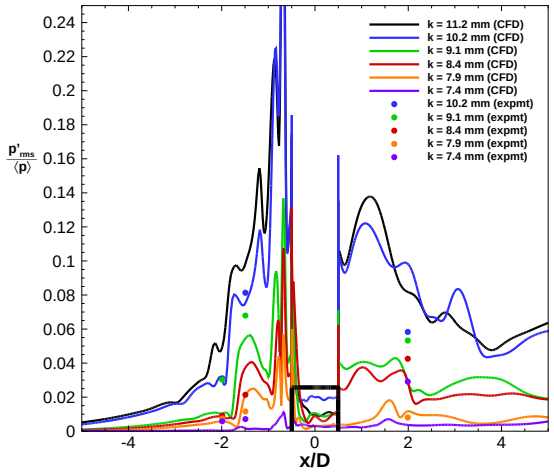

Figure 19. Computed and measured RMS pressure for various roughness heights along the centerline at the surface.

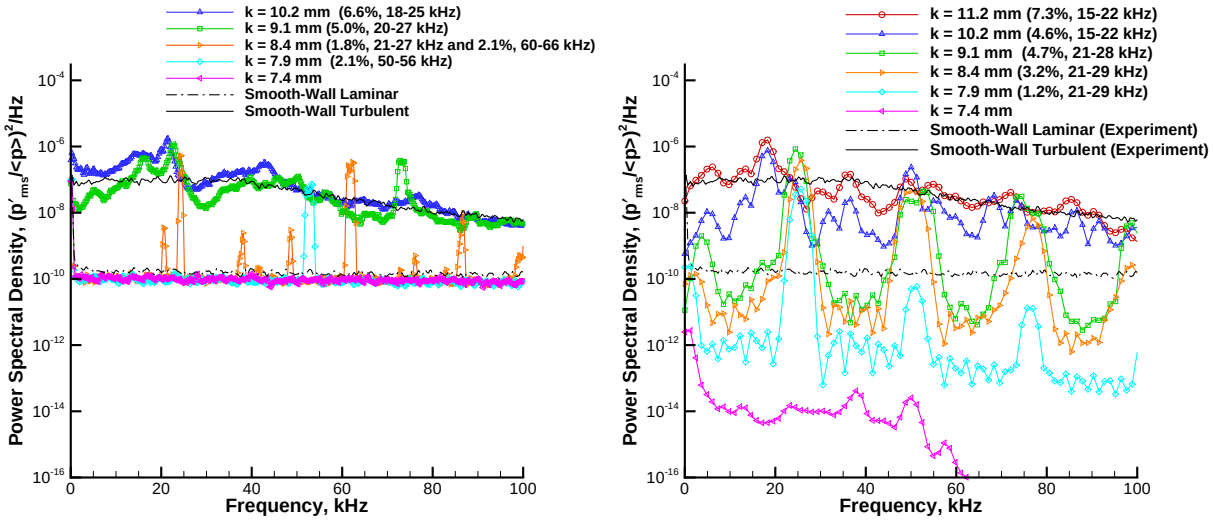

(a) Experiment

(b) CFD

Figure 20. Spectra at $x/D = -1.5$ showing the effect of roughness height on instabilities in the upstream separation region. The legend displays RMS/mean pressure taken from integrating under instability peaks. The range of integration is also shown.

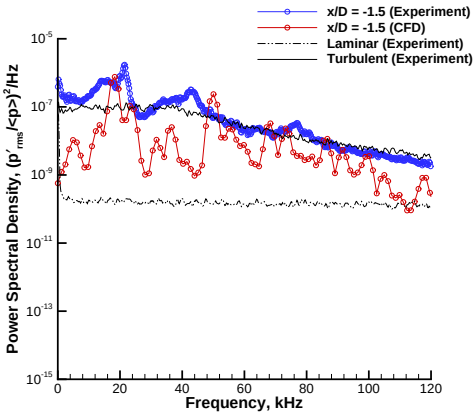

(a) $k = 10.2$ mm, $k/\delta = 1.23$, $Re_k = 7.0 \times 10^4$

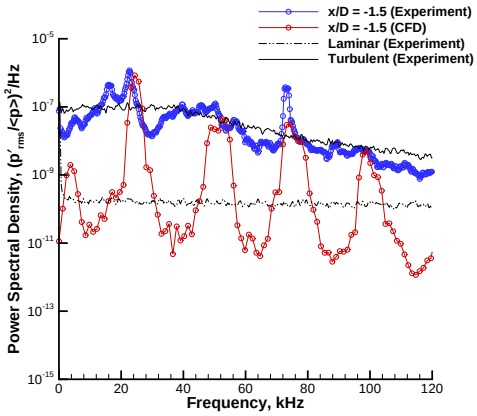

(b) $k = 9.1$ mm, $k/\delta = 1.10$, $Re_k = 6.2 \times 10^4$

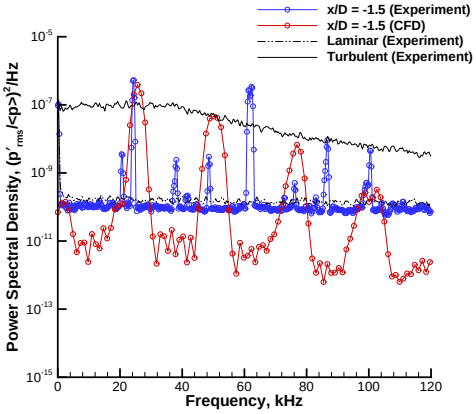

(c) $k = 8.4$ mm, $k/\delta = 1.01$, $Re_k = 5.3 \times 10^4$

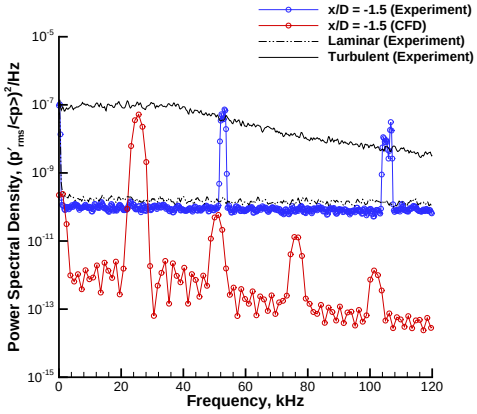

(d) $k = 7.9$ mm, $k/\delta = 0.95$, $Re_k = 4.1 \times 10^4$

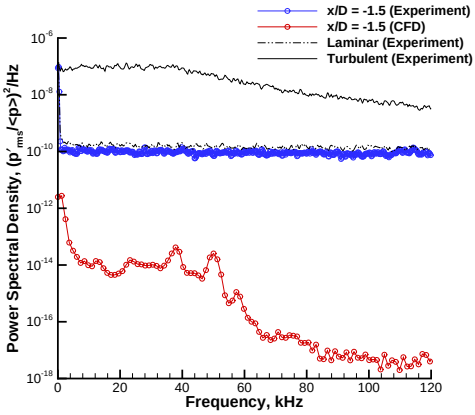

(e) $k = 7.4$ mm, $k/\delta = 0.89$, $Re_k = 2.7 \times 10^4$

Figure 21. Spectra at $x/D = -1.5$ showing the effect of roughness height on instabilities in the upstream separation region.

C. Summary of Roughness-Height Effects

When developing physics-based prediction methods for roughness-induced transition, changes in the dominant transition mechanism should be considered as the roughness height is reduced from large to small levels. Different mechanisms may require different methods of computational analysis. The effect of the cylindrical roughness height was examined here for a fixed Reynolds number. At a constant stagnation pressure of 90 psia, the instability mechanism appears to change at a condition of $Re_k \approx 6 \times 10^4$. Somewhere above this value, the dominant instability occurs at a frequency near 20-25 kHz due to the unsteady shock and separation structure upstream of the roughness. For roughness heights of 7.6–8.6 mm ($Re_k \approx 2$–6×10^4) a higher-frequency instability that was observed experimentally near 40–70 kHz was not seen in the CFD results. It is possible that this instability is excited by freestream disturbances that were not modeled in the simulation or that a much higher grid resolution would be required to capture it. For small roughness heights on the order of one fourth of the boundary-layer thickness, transition appears to occur at least sixty diameters downstream of the roughness. In these cases study of boundary-layer instabilities using DNS is not presently feasible due to the extremely large grid requirement.

VI. Summary

Transition due to roughness on the surface of a reentry vehicle can cause high levels of skin friction and heating in flight. Currently, empirical correlations are used by designers to predict the onset of transition, however these correlations can have large uncertainty. Future generations of prediction methods could be based upon the physical mechanisms responsible for roughness-induced transition, which are at present poorly understood. Moving toward development of physics-based prediction methods requires a greater understanding of these instability mechanisms. In the present work, controlled experimental measurements of instabilities were made in the wake of an isolated cylindrical roughness element within the laminar nozzle-wall boundary layer of the Boeing/AFOSR Mach-6 Quiet Tunnel at Purdue University. Flush-mounted pressure sensors within the wall were used to non-intrusively observe disturbances at specific locations. Direct numerical simulations of the flow were done at the University of Minnesota to examine the entire flow field at a level of detail not possible with experiments. The goal of this work was to directly compare the experimentally-observed and computed instabilities to determine the dominant mechanism for transition. A comparison of this type was not attempted previously at hypersonic speeds.

An instability with an experimentally-observed frequency near 21 kHz was studied for a specific roughness height of 10.2 mm. This height was roughly 1.2 times the boundary-layer thickness. The instability results from an unstable interaction between the bow shock (due to the roughness) and the separation shock (due to the separation bubble) region. High-pressure fluid in the post bow shock region is fed back into the separation bubble before convecting downstream into the wake, resulting in disturbances within the shear layer as well as in the horseshoe vortex structure. Though the frequency of the simulated instability was slightly lower than in the experiment (18 kHz), good agreement of the surface-pressure fluctuation amplitudes throughout the wake were obtained. Both experimental and CFD results showed evidence that the flow downstream of the roughness had transitioned. Because freestream noise was not simulated, it is likely that the instability is due solely to the roughness itself.

As the roughness height was reduced below 10.2 mm, a change in the dominant instability was observed by experiments within the upstream separation region. Below Re_k of approximately 6×10^4, a new higher-frequency instability was seen with lower broadband fluctuation levels. This second instability was not present in the simulations and it is thought this instability is more sensitive to the effect of the freestream disturbances that are not modeled in the simulations. As the roughness height was reduced, the experimental pressure fluctuations along the wake centerline indicated that transition moved downstream. Future experimental work will concentrate on studying instabilities which do not cause transition until far downstream of the roughness.

The present work has identified one of the instability mechanisms that contributes to transition for larger roughness heights. In addition, the work has predicted how this instability mechanism may change as the roughness height is reduced. Here, a "large" roughness is defined as a roughness of sufficient height to generate an absolute-like instability within the upstream separation region and transition relatively close to the roughness. It is now possible to perform a DNS to determine if a roughness is large enough to be an "effective" trip. Although such computations are far too costly for ordinary design purposes, these early results show they are feasible, and suggest they could determine sufficient (but not necessary) conditions

for effective trips. Additional experimental measurements and computations are needed for a wide range of conditions to build upon this work. In particular, stability calculations for different roughness heights would provide better understanding of these mechanisms. The end goal remains to develop improved transition-prediction methods that are feasible for use by designers, based on the growth of disturbances induced by the roughness.

Acknowledgments

The experimental work was sponsored by the NASA Fundamental Aeronautics program (grant 102361), NASA Constellation University Institutes Project (award Z634003), and the Air Force Office of Scientific Research (grant FA9550-09-1-0191). The computational work was sponsored by the Air Force Office of Scientific Research under grant FA9550-10-1-0352 and by the National Security Science and Engineering Faculty Fellowship.

References

[1]Kenneth F. Stetson. On Predicting Hypersonic Bounday Layer Transition. Technical Report AFWAL-TM-87-160-FIMG, Flight Dynamics Laboratory, Air Force Wright Aeronautical Laboratories, Wright-Patterson Air Force Base, Ohio, March 1987.

[2]Eli Reshotko. Transition Issues for Atmospheric Entry. *Journal of Spacecraft and Rockets*, 45(2):161–164, March-April 2008.

[3]Steven P. Schneider. Effects of Roughness on Hypersonic Boundary-Layer Transition. *Journal of Spacecraft and Rockets*, 45(2):193–209, March-April 2008.

[4]Scott A. Berry, Aaron H. Auslender, Arthur D. Dilley, and John F. Calleja. Hypersonic Boundary-Layer Trip Development for Hyper-X. *Journal of Spacecraft and Rockets*, 38(6):853–864, November-December 2001.

[5]Matthew P. Borg and Steven P. Schneider. Effect of Freestream Noise on Roughness-Induced Transition for the X-51A Forebody. *Journal of Spacecraft and Rockets*, 45(6):1106–1116, November-December 2008.

[6]Allen H. Whitehead. Flow Field and Drag Characteristics of Several Boundary-Layer Tripping Elements in Hypersonic Flow. Technical Report TN D-5454, NASA Langley Research Center, October 1969.

[7]Sandy C. Tirtey. *Characterization of a Transitional Hypersonic Boundary Layer in Wind Tunnel and Flight Conditions*. PhD thesis, Universite Libre de Bruxelles, October 2008.

[8]P. M. Danehy, C. B. Ivey, J. A. Inman, B. F. Bathel, S. B. Jones, A. C. McCrea, N. Jiang, M. Webster, W. Lempert, J. Miller, and T. Meyer. High-Speed PLIF Imaging of Hypersonic Transition over Discrete Cylindrical Roughness. AIAA Paper 2010-703, January 2010.

[9]Patrick Huerre and Peter A. Monkewitz. Local and Global Instabilities in Spatially Developing Flows. *Annual Review of Fluid Mechanics*, 22:473–537, 1990.

[10]M. S. Acarlar and C. R. Smith. A Study of Hairpin Vortices in a Laminar Boundary Layer. Part 1. Hairpin Vortices Generated by a Hemisphere Protuberance. *Journal of Fluid Mechanics*, 175:1–41, 1987.

[11]F. Gokhan Ergin and Edward B. White. Unsteady and Transitional Flows Behind Roughness Elements. *AIAA Journal*, 44(11):2504–2514, November 2006.

[12]Eli Reshotko and Anatoli Tumin. Role of Transient Growth in Roughness-Induced Transition. *AIAA Journal*, 42(4):766–770, April 2004.

[13]R. W. Wlezien. Measurements of Acoustic Receptivity. AIAA Paper 94-2221, June 1994.

[14]Daniel C. Reda. Review and Synthesis of Roughness-Dominated Transition Correlations for Reentry Applications. *Journal of Spacecraft and Rockets*, 39(2):161–167, March-April 2002.

[15]Charles H. Campbell, Rudolph A. King, Scott A. Berry, Michael A. Kegerise, and Thomas J. Horvath. Roles of Engineering Correlations in Hypersonic Entry Boundary Layer Transition Prediction. AIAA Paper 2010-0247, January 2010.

[16]Katya M. Casper, Heath B. Johnson, and Steven P. Schneider. Effect of Freestream Noise on Roughness-Induced Transition for a Slender Cone. *Journal of Spacecraft and Rockets*, 48(3):406–413, May-June 2011.

[17]Brian P. Anderson, Charles H. Campbell, Luis A. Saucedo, Gerald R. Kinder, and Karen T. Berger. Boundary Layer Transition Flight Experiment Overview and In-Situ Measurements. AIAA Paper 2010-0240, January 2010.

[18]Thomas J. Horvath, Deborah M. Tomek, Karen T. Berger, Scott C. Splinter, Joseph L. Zalameda, Paul W. Krasa, Steve Tack, Richard J. Schwartz, David M. Gibson, and Alan Tietjen. The HYTHIRM Project: Flight Thermography of the Space Shuttle During Hypersonic Re-Entry. AIAA Paper 2010-0241, January 2010.

[19]Hans W. Liepmann and Gertrude H. Fila. Investigations of Effects of Surface Temperature and Single Roughness Elements on Boundary-Layer Transition. NACA Report 890, 1947.

[20]P. S. Klebanoff and K. D. Tidstrom. Mechanism by Which a Two-Dimensional Roughness Element Induces Boundary-Layer Transition. *The Physics of Fluids*, 15(7):1173–1188, July 1972.

[21]Meelan Choudhari, Fei Li, and Jack Edwards. Stability Analysis of Roughness Array Wake in a High-Speed Boundary Layer. AIAA Paper 2009-0170, January 2009.

[22]Meelan Choudhari, Fei Li, Minwei Wu, Chau-Lyan Chang, and Jack Edwards. Laminar-Turbulent Transition behind Discrete Roughness Elements in a High-Speed Boundary Layer. AIAA Paper 2010-1575, January 2010.

[23]Chau-Lyan Chang, Meelan M. Choudhari, and Fei Li. Numerical Computations of Hypersonic Boundary-Layer over Surface Irregularities. AIAA Paper 2010-1572, January 2010.

[24]Matthew D. Bartkowicz, Pramod K. Subbareddy, and Graham V. Candler. Numerical Simulations of Roughness Induced Instability in the Purdue Mach 6 Wind Tunnel. AIAA Paper 2010-4723, June 2010.

[25]Michael A. Kegerise, Lewis R. Owens, and Rudolph A. King. High-Speed Boundary-Layer Transition Induced by an Isolated Roughness Element. AIAA Paper 2010-4999, June 2010.

[26]Bradley M. Wheaton and Steven P. Schneider. Roughness-Induced Instability in a Laminar Boundary Layer at Mach 6. AIAA Paper 2010-1574, January 2010.

[27]Brad M. Wheaton, Thomas J. Juliano, Dennis C. Berridge, Amanda Chou, Peter L. Gilbert, Katya M. Casper, Laura E. Steen, Steven P. Schneider, and Heath B. Johnson. Instability and Transition Measurements in the Mach-6 Quiet Tunnel. AIAA Paper 2009-3559, June 2009.

[28]Bradley M. Wheaton. Roughness-Induced Instability in a Laminar Boundary Layer at Mach 6. Master's thesis, Purdue University School of Aeronautics & Astronautics, West Lafayette, IN, December 2009.

[29]Christopher A. C. Ward, Bradley M. Wheaton, Amanda Chou, Peter L. Gilbert, Laura E. Steen, and Steven P. Schneider. Boundary-Layer Transition Measurements in a Mach-6 Quiet Tunnel. AIAA Paper 2010-4721, June 2010.

[30]Amanda Chou, Bradley M. Wheaton, Christopher A. C. Ward, Peter L. Gilbert, Laura E. Steen, and Steven P. Schneider. Instability and Transition Research in a Mach-6 Quiet Tunnel. AIAA Paper 2011-283, January 2011.

[31]Thomas J. Juliano, Steven P. Schneider, Selin Aradag, and Doyle Knight. Quiet-Flow Ludwieg Tube for Hypersonic Transition Research. *AIAA Journal*, 46(7):1757–1763, July 2008.

[32]I. Beckwith, F. Chen, S. Wilkinson, M. Malik, and D. Tuttle. Design and Operational Features of Low-Disturbance Wind Tunnels at NASA Langley for Mach Numbers from 3.5 to 18. AIAA Paper 90-1391, June 1990.

[33]Jerrod W. Hofferth, Rodney D. W. Bowersox, and William S. Saric. The Mach 6 Quiet Tunnel at Texas A&M: Quiet Flow Performance. AIAA Paper 2010-4794, June 2010.

[34]Steven P. Schneider. Design of a Mach-6 Quiet-flow Wind Tunnel Nozzle using the e**N Method for Transition Estimation. AIAA Paper 1998-0547, January 1998.

[35]Steven J. Beresh, John F. Henfling, Russell W. Spillers, and Brian O. M. Pruett. Measurement of Fluctuating Wall Pressures Beneath a Supersonic Turbulent Boundary Layer. AIAA Paper 2010-0305, January 2010.

[36]Katya M. Casper, Steven J. Beresh, and Steven P. Schneider. Pressure Fluctuations Beneath Turbulent Spots and Instability Wave Packets in a Hypersonic Boundary Layer. AIAA Paper 2011-372, January 2011.

[37]Ioannis Nompelis, Travis W. Drayna, and Graham V. Candler. A Parallel Unstructured Implicit Solver for Reacting Flow Simulation. AIAA Paper 2005-4867, 2005.

[38]Pramod K. Subbareddy and Graham V. Candler. A Fully Discrete, Kinetic Energy Consistent Finite-Volume Scheme for Compressible Flows. *Journal of Computational Physics*, 228:1347–1364, 2009.

[39]Y. Ren M. Liu and H. Zhang. A Characteristic-Wise Hybrid Compact-WENO Scheme for Solving Hyperbolic Conservation Laws. *J. Comp. Phys.*, 192:365–386, 2003.

[40]Michael J. Wright, Graham V. Candler, and M. Prampolini. Data Parallel Lower-Upper Relaxation Method for the Navier-Stokes Equations. *AIAA Journal*, 34:1371–1377, 1996.

[41]C. J. Baker. The Laminar Horseshoe Vortex. *Journal of Fluid Mechanics*, 95:347–367, 1979.

[42]D. J. Maull. Hypersonic flow over axially symmetric spike bodies. *Journal of Fluid Mechanics*, 8:584–592, 1960.

[43]Daniel Feszty, Ken J. Badcock, and Bryan E. Richards. Driving Mechanisms of High-Speed Unsteady Spiked Body Flows, Part 1: Pulsation Mode. *AIAA Journal*, 42:95–106, 2004.

[44]P. R. Spalart. Direct Simulation of a Turbulent Boundary Layer up to $R_\theta = 1440$. *Journal of Fluid Mechanics*, 187:61–98, 1988.

[45]J. Murlis, H.M. Tsai, and P. Bradshaw. The Structure of Turbulent Boundary Layers at Low Reynolds Numbers. *Journal of Fluid Mechanics*, 122:13–56, 1982.

[46]Julius E. Harris and Doris K. Blanchard. Computer Program for Solving Laminar, Transitional, or Turbulent Compressible Boundary-Layer Equations for Two-Dimensional and Axisymmetric Flow. NASA Technical Report TM-83207, February 1982.

[47]A. Martellucci, L. Chaump, and D. Rogers. Experimental Determination of the Aeroacoustic Environment about a Slender Cone. *AIAA Journal*, 11(5):634–642, May 1973.